LL

EUROPEAN ORGANIZATION FOR NUCLEAR RESEARCH

CERN LIBRARIES, GENEVA

CERN-AT-94-46

CERN AT/94-46 (CR)
LHC Note 307

SE 9506

Investigation of Quench Pressure Transients in the LHC Superconducting Magnets

Thomas Wahlström

Abstract

In case of resistive transition of a LHC superconducting magnet ("quench"), the stored energy is dissipated in the winding within a few tenths of a second. A fraction of this energy is transferred to the helium inside the windings and around the beam tubes, causing expansion and axial flow to the end reservoirs of the cryostat helium vessel, where it is finally discharged through a relief valve. This thermo-hydraulic process gives rise to a fast pressure peak at the midlength of the magnet, and a more gradual pressure rise in the end reservoirs.

It will be presented here as a one-dimensional thermo-hydraulic model aimed at simulation of the quench pressure peak and to study the influence of geometrical parameters, such as magnet length and beam pipe diameter. Results of the simulations are compared to measurements performed on a short model and on two quasi-full scale prototypes of the LHC dipoles.

Geneva, Switzerland
20 December 1994

Contents

1. INTRODUCTION

The Large Hadron Collider (LHC) at CERN [1] is currently undergoing design studies and development work. The collider, operating in the TeV-range, will consist of a single ring of twin-aperture superconducting magnets using NbTi-conductors and operating in static baths of pressurised superfluid helium at 1.9 K and 0.1 MPa. The present prototype dipole magnets are about 10 m long, 560 mm in diameter with an aperture diameter of 50 mm (Appendix A).

While ramping up the current and during normal operation, a dipole may undergo resistive transition, called quench, where the stored energy of several MJ per magnet is dissipated in the windings within a few tenths of a second. A fraction of this energy is transferred to the helium inside the porous windings and to the annular space around the beam tubes (figure 1.1,1.2), causing expansion and axial flow to the end reservoirs of the cryostat helium vessel, where it is finally discharged through a relief valve. This thermo-hydraulic process gives rise to a pressure peak at the midlength of the magnet with a magnitude of several tens of bars, and a rise time of a few tenths of a second, and is followed by a more gradual pressure rise in the end volumes and later a decline due to the opening of the relief valve.

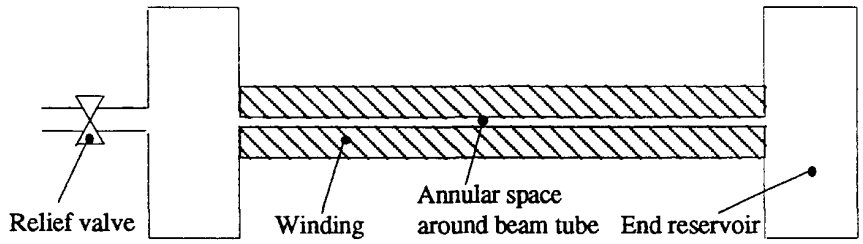

Figure 1.1 Dipole magnet

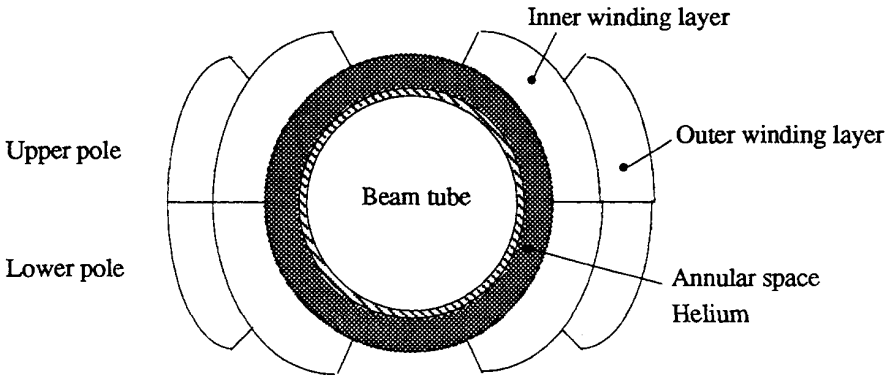

Figure 1.2 Dipole aperture

Figure 1.3 shows measurements of these pressure transients provoked by a quench occurring in a 10 m long LHC prototype dipole. Analysis of both pressure transients is important, as the initial peak may cause buckling of the beam tube and the pressure rise in the end reservoirs defines the size and the response time of the relief valve. The magnet length and the annular space between the beam pipe and the winding, defined

by the outer beam pipe diameter, are fundamental geometrical design parameters affecting the pressure transients. The final design of the LHC dipole magnet is at present not fully finalised, however the current trend is towards increasing magnet length.

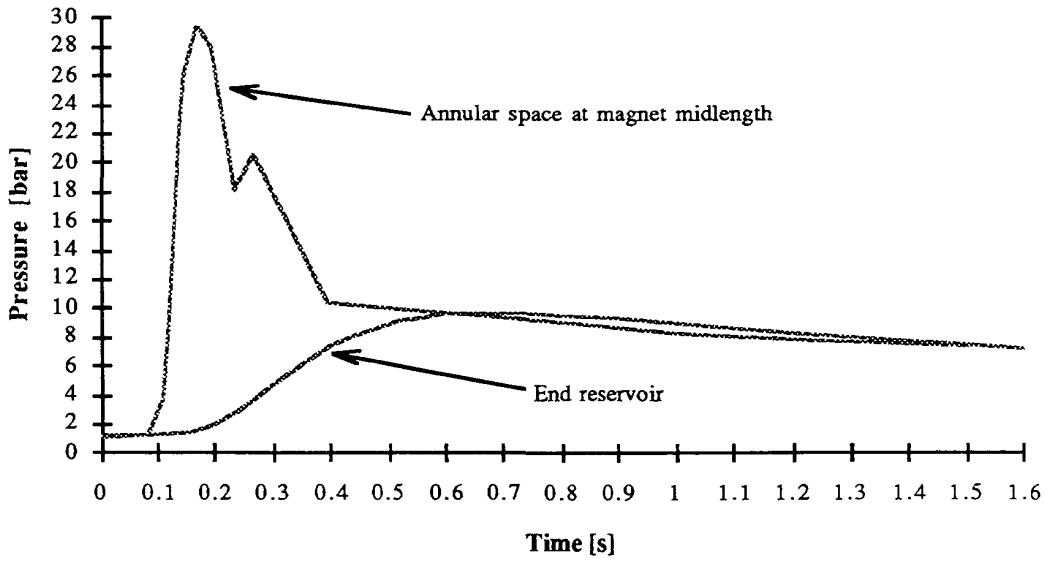

Figure 1.3 Measured quench pressure transients

A study of the pressure transients due to quench is here presented. The study was made by means of a one-dimensional thermo-hydraulic simulation model, and the results are compared with measurements performed on a short 1 m model and on two quasi-full scale prototypes of the LHC dipoles, the Twin-Aperture Prototype (TAP) and the INFN2 dipole. The effect of magnet length and the annular space on the pressure peak is presented.

2. SIMULATION MODEL

2.1 THE MODELLED SYSTEM

The one-dimensional modelled system is shown in figure 2.1. Only one of the two dipoles in the twin aperture magnet is modelled. Half the total end reservoir volume, half the cross-section of the collars and the yoke, and half the cross-section of the relief pipe and the valve are taken into account. The solid parts of the system (the winding, the insulation, the collars and the yoke) are considered as lumped. The relief valve is modelled as a restriction in the relief pipe and the outlet from the relief pipe is to constant pressure of 1.2 bars.

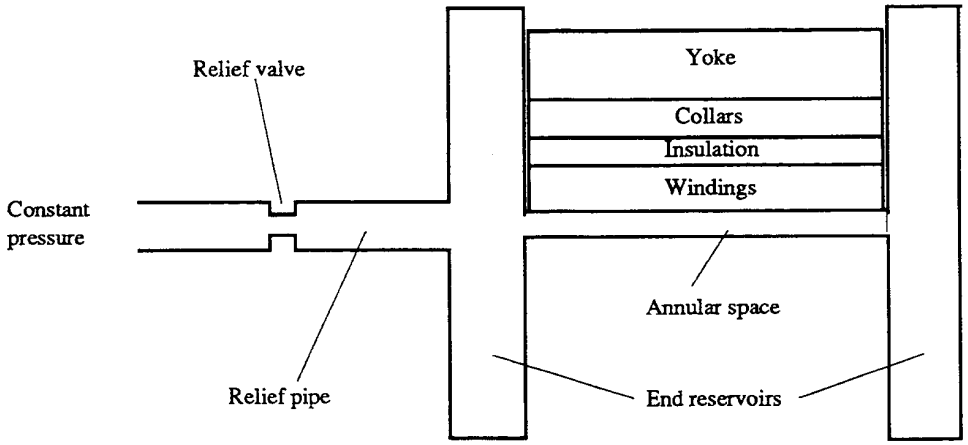

Figure 2.1 The one-dimensional thermo-hydraulic simulation model

2.1 ASSUMPTIONS

Several assumptions are made in the modelling of the thermodynamic and hydraulic process followed by a quench of the superconducting dipole. The assumptions are as follows:

Quench propagation

After the initiation of a quench, the small resistive region either recovers to super-conducting state or starts to naturally propagate longitudinally and transversally in the winding. If the latter alternative occurs, the quench is detected and the quench heaters glued on the outer layers of the winding will be fired after a time delay, which will quench the outer layers uniformly. In the model it is assumed that the energy dissipation in the winding, inner and outer layers, is uniform and starts at the time of the quench initiation.

Helium expulsion from the winding

A part of the energy dissipated in the winding will be transferred to the helium inside the porous winding. The helium expands and a part of it is probably expelled into the

annular space around the beam tube. The expulsion of helium is neglected in the model.

Radial venting

The windings are assembled in collars, and a iron yoke surrounds the two collared dipoles, see Appendix A. Due to the collars and the yoke being laminated the helium in the annular space around the beam tubes might be able to vent radially, followed by longitudinally venting through holes in the yoke structure to the two end reservoirs. The possibility of radial venting of helium is neglected.

Heat transfer from the winding to the helium in the annular space

The heat transfer from the winding to the helium in the annular space around the beam tube is modelled as solid conduction through the superconducting cable insulation. The possibility of heat transfer by thermal conduction in helium is neglected, since the helium becomes gaseous very soon, with a low thermal conductivity.

Thermal conduction in helium

Longitudinal thermal conduction in helium in the annular space is negligible and is therefore neglected in the model.

The annular space around the beam tube

The annular space is determined by the inner diameter of the inner layer of the winding, i.e. the aperture diameter, and the outer diameter of the beam tube, and is modelled as a tube with the corresponding hydraulic diameter.

2.3 MATHEMATICAL DESCRIPTION

The one-dimensional thermo-hydraulic simulation model is governed by four partial differential equations. The helium flow is governed by the equations of continuity, momentum and energy conservation and the winding, the collars, the insulation and the yoke by the equation of energy conservation. The helium flow is modelled as being homogeneous.

2.3.1 Conservation of momentum

The equation for conservation of momentum is

$$\frac{\partial(\rho u)}{\partial t}+\frac{\partial(\rho u^2)}{\partial x} = -\frac{\partial P}{\partial x} - \frac{\partial P}{\partial x}\Big|_{fr} - \frac{\partial P}{\partial x}\Big|_{A} \tag{2.1}$$

where

$$\frac{\partial P}{\partial x}\Big|_{fr} = \frac{\lambda}{D_h}\rho\frac{u}{2}|u| \tag{2.2}$$

$$\frac{\partial P}{\partial x}\Big|_{A} = \frac{\xi}{\Delta x}\rho\frac{u}{2}|u| \tag{2.3}$$

The first term in (2.1) is the transient term and the second the divergence term. Equation (2.2) expresses the pressure drop per unit length due to flow friction between the fluid and the tube wall and (2.3) the pressure drop per unit length due to abrupt changes in tube cross-section.

2.3.2 Continuity equation

The conservation of mass is expressed in the continuity equation (2.4).

$$\frac{\partial \rho}{\partial t} + \frac{\partial (\rho u)}{\partial x} = 0 \tag{2.4}$$

Equation (2.4) is by means of the momentum equation turned into an equation for pressure correction [3]. In this way the guessed pressure field in the momentum equation can be corrected so the velocity field, determined by the momentum equation, will progressively get closer to satisfying the continuity equation.

2.3.3 Conservation of energy of the helium

The equation for energy conservation of the helium can be written as (2.5)

$$\frac{\partial (\rho e)}{\partial t} + \frac{\partial (\rho u e)}{\partial x} = -P\frac{\partial u}{\partial x} + \frac{\lambda}{D_h}\rho\frac{u^2}{2}|u| + \frac{\xi}{\Delta x}\rho\frac{u^2}{2}|u| - \frac{\partial q_c}{\partial x} + \varphi + \omega \tag{2.5}$$

where the first term on right side represents the flow work, the second the power dissipation due to frictional flow, the third the power dissipation due to turbulent eddies caused by abrupt change in tube cross-section, the fourth represents axial thermal conduction, the fifth term φ is the internal power generation and the last term ω is the heat convected from the tube wall (winding) to the helium. The convection term is expressed as

$$\omega = \frac{h}{\Delta x A} \cdot \alpha S \cdot (T_s - T_b) \tag{2.6}$$

where T_S is the surface temperature and T_b the bath temperature.
The axial thermal conduction is neglected and the internal power generation is zero.

2.3.4 Conservation of energy of the solid parts

The solid parts in the model are the winding, the collars, the yoke and the insulation between the winding and the collars. The governing equation is the equation for conservation of energy and is written as

$$\rho c \frac{\partial T}{\partial t} = k\frac{\partial^2 T}{\partial x^2} + \varphi + \omega \tag{2.7}$$

where the first term on the right side is the power conducted between the different solid parts, the second term the internal power generation and the third term is the heat convection. The power dissipation in the winding due to the quench is expressed by the internal power generation term and the heat transferred from the winding to the helium in the annular space around the beam tube is expressed by the convection term.

2.4 POWER DISSIPATION IN THE WINDING

The power dissipation in the winding is calculated from measurements of the current decay in the winding and the voltage across the poles or layers of the winding during the quench. The self and mutual inductance of the dipoles, the poles and the layers are also measured.
From these measurements the resistance in the winding can be calculated from (2.8)

$$R_{winding} = \frac{1}{I_{winding}} \cdot \left\{ U_{winding} + \left(L_{winding} + \sum M \right) \frac{dI_{winding}}{dt} \right\} \tag{2.8}$$

and then power dissipation in the winding is then

$$Q_{winding} = R_{winding} \cdot I^2_{winding} \tag{2.9}$$

The power dissipation can be calculated per layer or pole depending upon the available voltage measurements. Calculation of, for example, the power dissipation in a layer requires of course the voltage measurement across the actual layer. The voltage measurements are different depending on the dipole test.

2.5 CONVECTIVE HEAT TRANSFER COEFFICIENT

The convective heat transfer coefficient for the heat transfer from the winding to the helium in the annular space around the beam tube is derived from the thermal conductivity of the superconducting cable insulation. The cable insulation is generally made up as in figure 2.2.

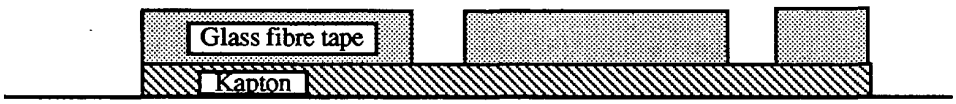

Figure 2.2 Superconducting cable insulation

The cable is first wrapped by one or several overlapping layers of Kapton. Above there is a thick glass fibre tape (in order of 100μm) wrapped with a few millimetres space between each turn. The equivalent thermal conductivity of the layers of Kapton and glass fibre tape is

$$k_{eq} = k_{Kapton} \cdot k_{GF} \frac{k_{Kapton} \cdot k_{GF} \left(\delta_{Kapton} + \delta_{GF} \right)}{k_{GF} \delta_{Kapton} + k_{Kapton} \delta_{GF}} \tag{2.10}$$

The power conducted through the layers of Kapton and glass fibre tape over the temperature difference dT, is then

$$Q = -k_{eq} S_{GF} \frac{dT}{\delta_{Kapton} + \delta_{GF}} \tag{2.11}$$

The power conducted through a slab of material assuming steady state is equal to the power convected away from the surface of the slab. The following relation can be established

$$kS\frac{dT}{\delta} = hSdT \tag{2.12}$$

Inserting on the left side of (2.12) the power conducted through the layers of Kapton and glass fibre tape plus the power conducted through the Kapton layer in the space between the glass fibre wrapping over the temperature difference dT, gives the overall heat transfer coefficient h.

$$h = \frac{k_{eq}\dfrac{S_{GF}}{\delta_{Kapton}+\delta_{GF}} + k_{Kapton}\dfrac{S_{Kapton}}{\delta_{Kapton}}}{S_{GF}+S_{Kapton}} \tag{2.13}$$

The thermal conductivity of the Kapton and the glass fibre tape depends on the winding temperature.

2.6 HEAT TRANSFER AREA AND MULTIPLICATION FACTOR

The geometrical heat transfer area of the heat convected from the winding to the helium in the annular space around the beam tube is the surface of the cylindrical aperture occupied by the superconducting cable. A free chosen multiplication factor, α, is used in the relation governing the convection of heat from the winding to the helium in the annular space, (2.6), to enable fit of the simulated pressure transient at magnet midlength to the measurement. The multiplication factor in the model is the only free parameter, and it combines several uncertainties, the surface of the cable taking part in the heat transfer, the growth of the heat transfer area as function of time and the thermal conductivity of the cable insulation.

2.7 FLOW FRICTION

The viscous friction due to flow is taken into account, and the friction factor is dependent on the Reynolds number and the relative roughness of the tube, and determined from Moody's diagram.

The following empirical formulae for different flow regimes are used to determine the friction factor ;

Laminar

$$\lambda = \frac{96}{Re_D} \qquad 0 < Re_D < 2000 \tag{2.14}$$

The formula is for laminar flow between two concentric cylindrical rough tubes.

Turbulent flow

$$\frac{1}{\sqrt{\lambda}} = -3.6\log_{10}\left(\frac{6.9}{Re_D} + \left(\frac{\varepsilon}{3.71 \cdot D_h}\right)^{1.11}\right) \qquad Re_D > 4000 \qquad (2.15)$$

The empirical relation (2.15) is referenced to S.E. Haaland [4].

Critical regime

The critical regime is $2000 < Re_D < 4000$ and the friction coefficient is determined as a linear interpolation between the laminar and the turbulent regimes.

Since the helium has very low viscosity the flow becomes strongly turbulent even for small velocities. Reynolds number is in the order of 10^5-10^6. The roughness ε is 0.045 mm in the simulations, giving a friction factor in accordance with measurements carried out on the short twin aperture dipole model.

2.7 THERMO-PHYSICAL PROPERTIES OF HELIUM

The thermo-physical properties of helium is during the simulation calculated by the program HEPAK [5], which has an interface to the simulation code. Two properties of the helium are the input to HEPAK and it calculates the other properties required.

3. SIMULATION CODE

3.1 DISCRETISATION

The hydraulic part of the model is discretized one-dimensionally into a certain number of pressure nodes, each with a corresponding finite volume (control volume). All the thermo-physical properties of the helium are determined in the pressure nodes. The velocities are determined in the velocity nodes, which are staggered in comparison to the pressure nodes, which can be seen in figure 3.1, where the capital letters represent the pressure nodes and the small case letters the velocity nodes. The control volume of the pressure node P and the velocity node e is shown as a solid and a dashed square respectively.

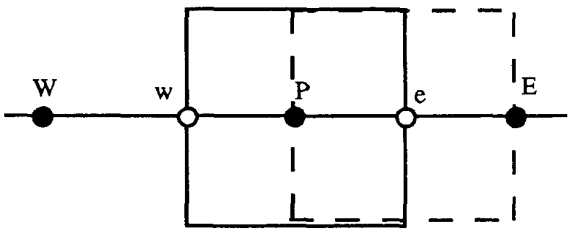

Figure 2.2 Pressure and velocity nodes

Each of the solid part of the model, the winding, the insulation, the collars and the yoke are considered as lumped and discretized by one temperature node each.

The four partial differential equations describing the thermo-hydraulic quench process are integrated over the appropriate control volume and discretized by the finite difference method in an implicit upwind scheme [2,3].

3.2 SOLUTION ALGORITHM

The solution algorithm for calculating the flow field is called SIMPLE (Simple-Implicit Method for Pressure Linked Equations) [3, pp 126].

The main steps in the SIMPLE-algorithm in the order of their execution, are :

1. Guess a pressure field $\overline{P}^*$.

2. Solve the discretized momentum equations to obtain the velocity field $\overline{u}^*$.

3. Solve the discretized pressure-correction equations (transformed continuity equations, see §2.3.2) to obtain the field of pressure corrections $\overline{P}'$.

4. Correct the pressure field : $\overline{P} = \overline{P}^* + \overline{P}'$

5. Correct the velocity field : $\overline{u} = \overline{u}^* + \overline{u}'(\overline{P}')$

6. Solve the discretized equations for energy conservation to obtain the specific internal energy in the discretisation nodes of the flow field.

7. Treat the corrected pressure field $\overline{P}$ as a new guessed pressure field $\overline{P}^*$ and return to step 2 and repeat the whole procedure until a converged solution is obtained.

The discretized equations in step 2,3 and 6 are solved iteratively by means of the Gauss-Seidel point-by-point method [3,pp 62]. This is a simple iterative method in which the values of the variable are calculated by visiting each discretisation point, e.g. a pressure node, in a certain order. When all the nodes have been visited, one iteration has been done, and if convergence is not obtained, the first node is visited again, but with values of the variable determined in the previous iteration. In this way the values of the variable will progressively get closer to the solution.

After the flow field has converged the temperature field of the solid part of the model has to be determined. The set of the discretized equations for conservation of energy are solved by means of Gauss-Elimination of the equation system. This is a simple way of solution without iterations, since the temperature field consists of only four unknowns.

If the temperature field has not converged, the procedure of determining the flow field and the temperature field has to be performed again. The whole solution algorithm for the flow and the temperature field is shown schematically in figure 3.2.

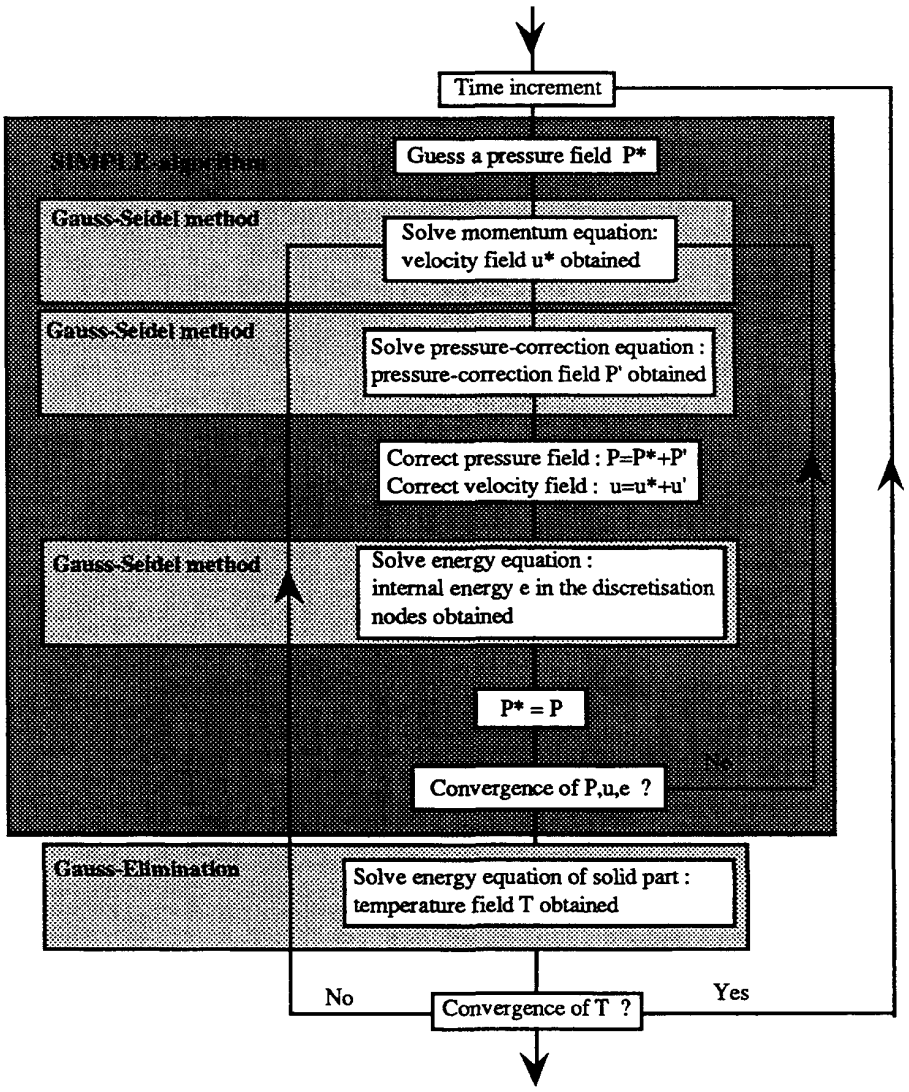

Figure 3.2 Solution algorithm

3.3 REMARKS

The simulation program is written in the language Fortran 77. The simulations are performed in CSF [6] (Central Simulation Facility), which uses a cluster of 25 HP 9000/720 workstations.

4. SIMULATIONS AND MEASUREMENTS

The pressure transients due to quench have been studied on three different twin aperture LHC dipoles, where two of them are quasi-full scale prototypes and the third is a short 1 m model.

4.1 THE TWIN-APERTURE PROTOTYPE

4.1.1 Magnet data

The Twin-Aperture Prototype (TAP) [7] is a quasi-full scale twin aperture dipole prototype designed by CERN and tested at CEN, Saclay in France. The most important magnetic and geometric data are summarised in table 4.1.

Self inductance / dipole	55	mH
Magnetic length	9.1	m
Magnet diameter	0.59	m
Annular length	9.1	m
Aperture diameter	75	mm
Beam tube outer diameter	70.5	mm
Annular space	2.25	mm
Winding mass/dipole	235	kg
Winding mass inner layer/dipole	87	kg
Winding mass outer layer/dipole	148	kg
Helium volume in annular space	4.7	litres
Helium volume of reservoirs/magnet	136	litres

Table 4.1 TAP magnet data

4.1.2 Measurements

The pressure transients due to quench from different excitation currents have been measured in the annular space at magnet midlength and in the two end reservoirs [8]. The pressure transients during a few quenches at different excitation currents have been studied (table 4.2).

I_o	E_{magn}	B_o
[A]	[MJ]	[T]
5530	0.8	no data
6960	1.3	no data
8820	2.1	7.74
9505	2.5	8.25

Table 4.2 Quenches

I_o is the quench current, E_{magn} the stored energy in one dipole and B_o the central magnetic field. The quenches in table 4.2 are all at the helium bath temperature of 1.8K. The measured current decay during the quenches for different excitation currents are shown in figure 4.1. The measured pressure transient, in the annular space of one of the apertures at magnet midlength, at different quench currents, is shown in figure 4.2. The pressure rise in the other aperture is only slightly different in time and magnitude. The rise time, between initiation of quench and peak pressure, was measured at 150 ms for the quench at current 9505 A. The rise time decreases with decreasing excitation current as seen in figure 4.2. The magnitude of the pressure peak at different quench currents shows a linear dependency on the stored magnetic energy.

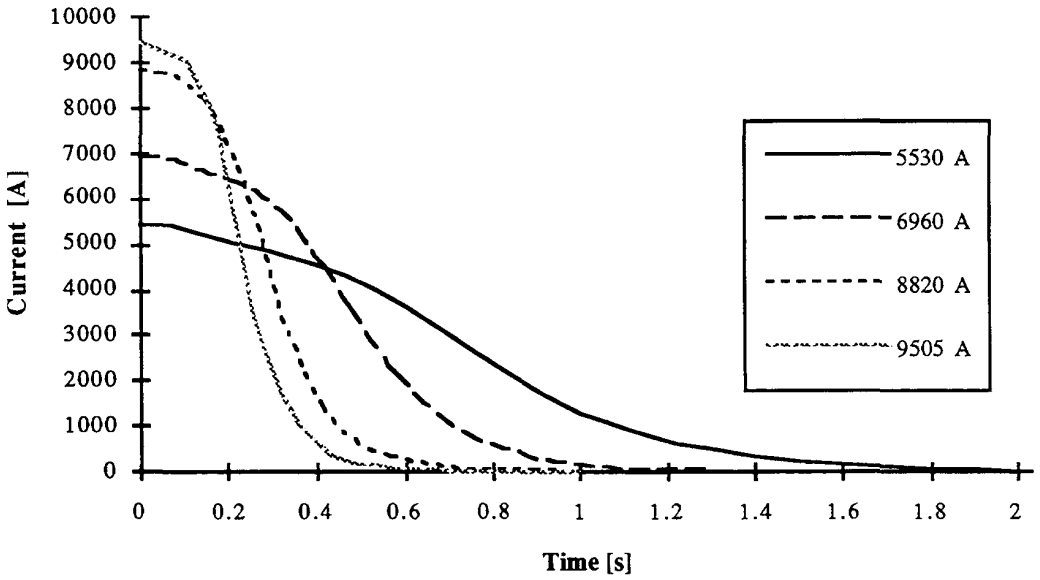

Figure 4.1 Measured current decay during quench at different quench currents

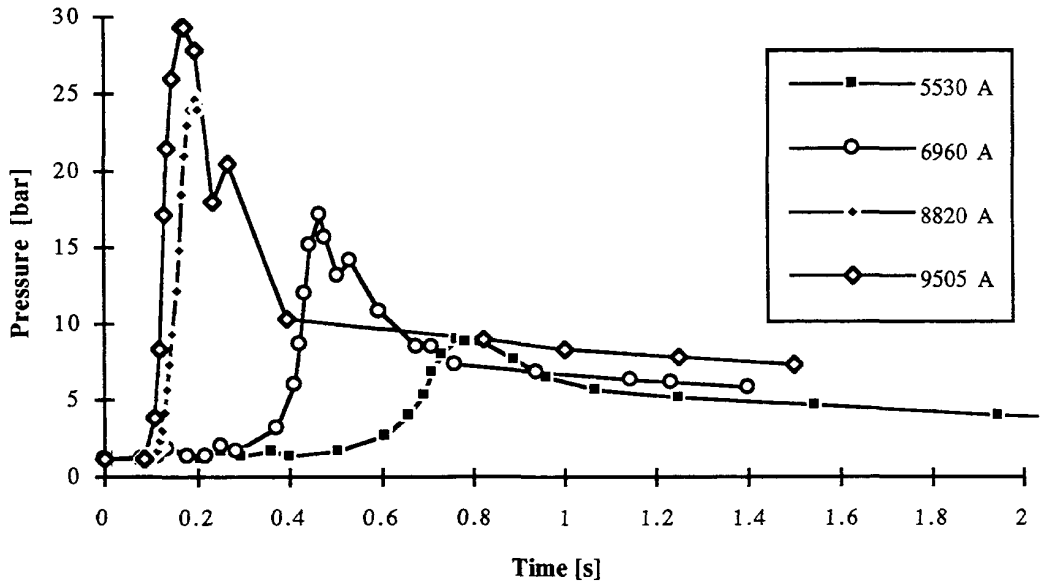

Figure 4.2 Measured pressure transient in the annular space at magnet midlength at different quench currents

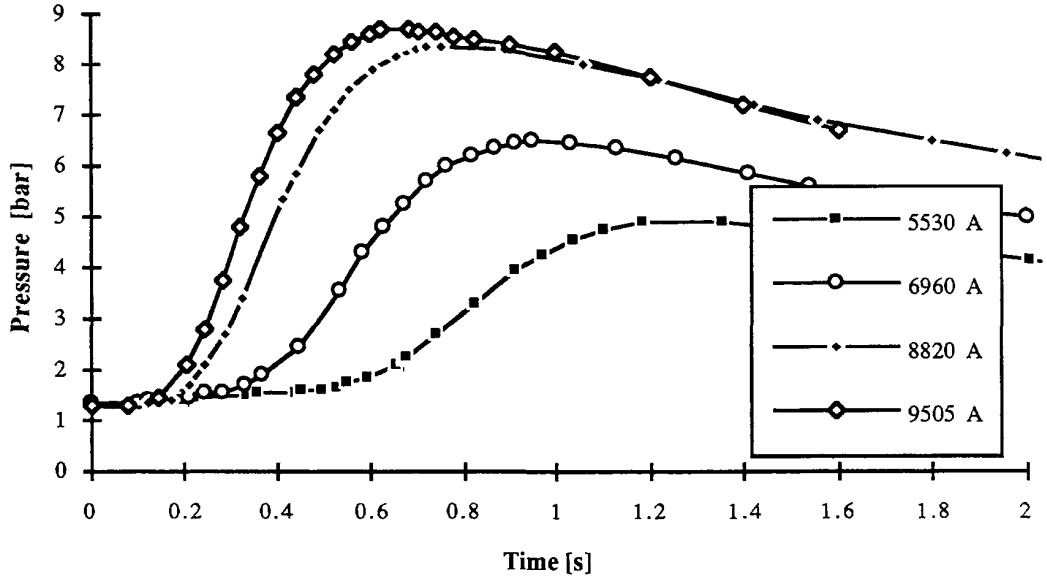

Figure 4.3 Measured pressure rise in the end reservoir next to the discharge valve at different quench currents

Figure 4.3 shows the measured pressure rise in the end reservoir next to the relief valve during a quench, at different quench currents. The pressure in the other end reservoir evolves in the same way but the magnitude is slightly larger, in order of 1 bar. The relief valve starts to open 30 ms after the quench detection and the time until it is fully open is in the order of 100 ms. The quench detection time is less then 50 ms, which means that the valve is fully open at about 0.2 s.

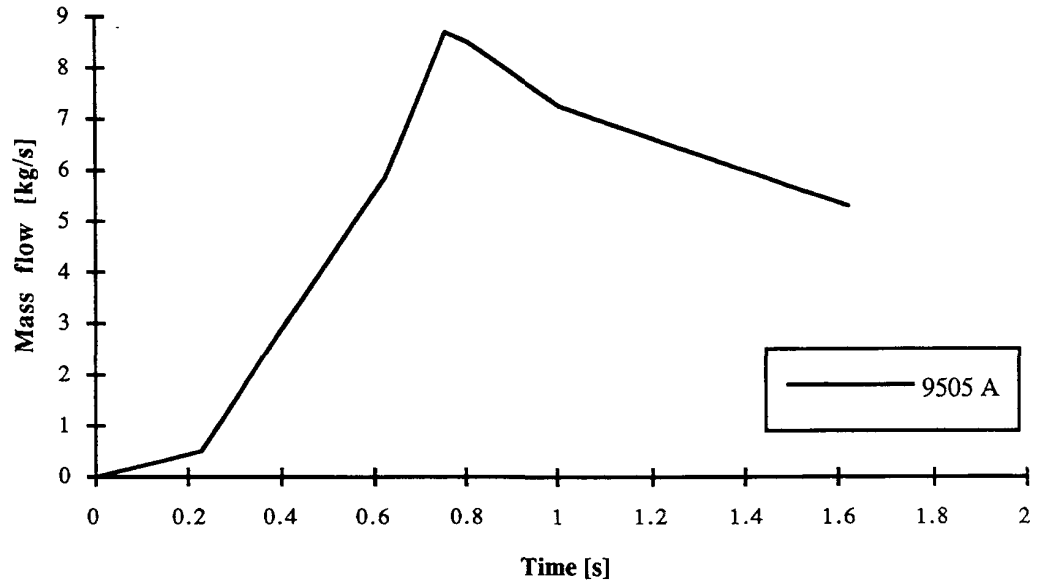

Figure 4.4 Mass flow measured after the relief valve

Figure 4.4 shows the measured mass flow after the relief valve during the quench at 9505 A. The mass flow is calculated from the dynamic pressure measured by a Pitot tube, and the maximum coincides with the maximum pressure in the end reservoirs.

4.1.3 Simulation results

The results from the simulation of the quench at excitation current 9505 A will be presented here in detail. The results of the remaining three quenches listed in table 4.2 will only be commented upon briefly.

A. Dissipation of energy in the winding

The growth of the resistance in the dipole winding during the quench, calculated from equation (2.8), is shown in figure 4.5. The resistance is calculated per pole and the dipole resistance is the sum of the two pole resistance.

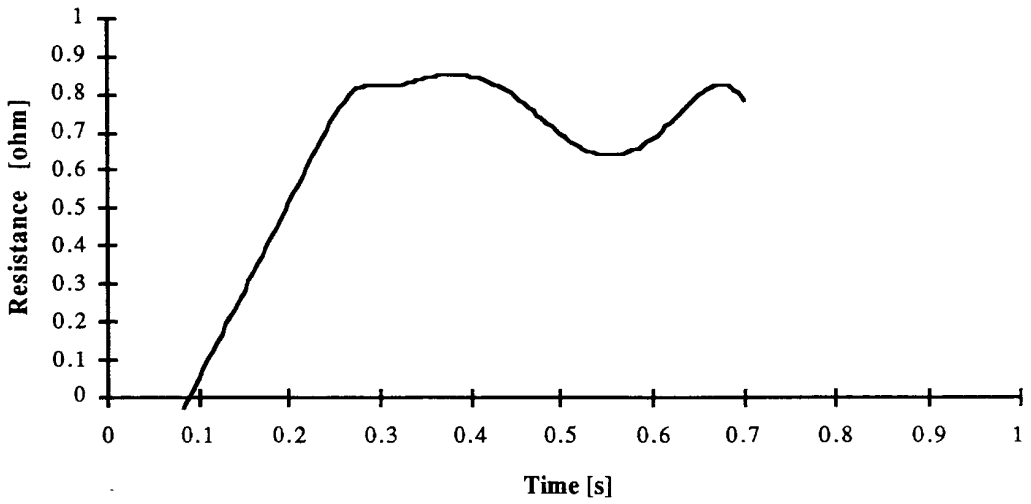

Figure 4.5 Dipole resistance

The power dissipation is calculated per pole from equation (2.9) and the dissipation in the dipole is the sum of the dissipation in the two poles, see figure 4.6. The maximum power dissipation is 16 MW after 190 ms, which nearly coincides with the time of the pressure peak, 170 ms (figure 4.2). This coincidence has been observed in all four quenches studied.

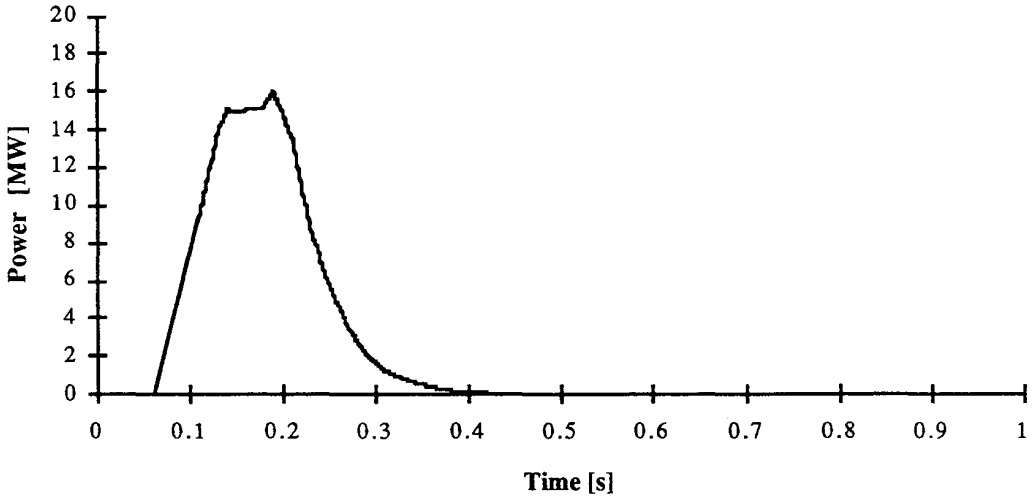

Figure 4.6 Power dissipation in the dipole winding

B. Power transferred from the winding to the helium in the annular space

The total power transferred from the winding to the helium in the annular space around the beam tube depends on the convective heat transfer coefficient, winding and helium temperatures and the heat transfer area, equation (2.6). The convected power is shown in figure 4.7, and the maximum value is 480 kW after 210 ms. The spatial distribution of the convected power along the annular is parabolic with the maximum at magnet midlength.

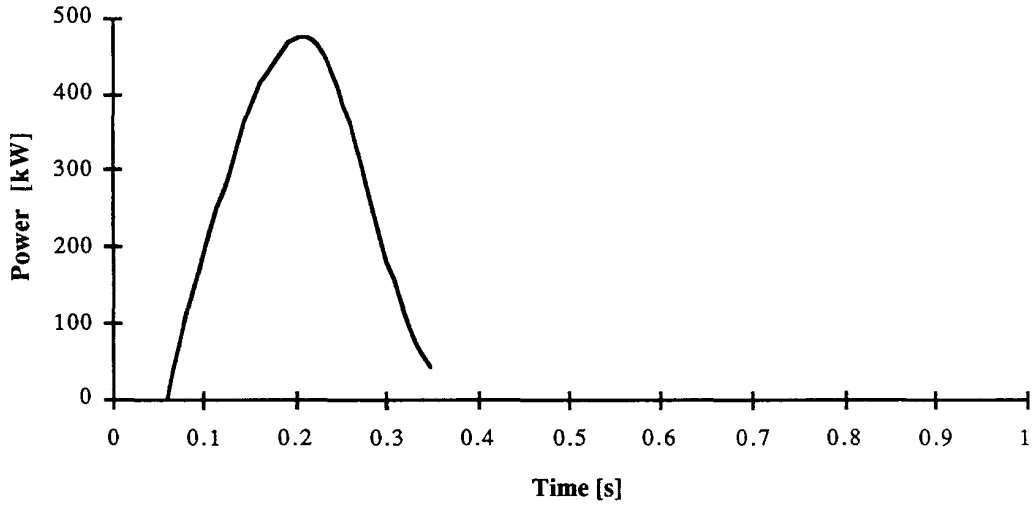

Figure 4.7 Total convected power from the winding to the helium in the annular space

C. Winding and helium temperature

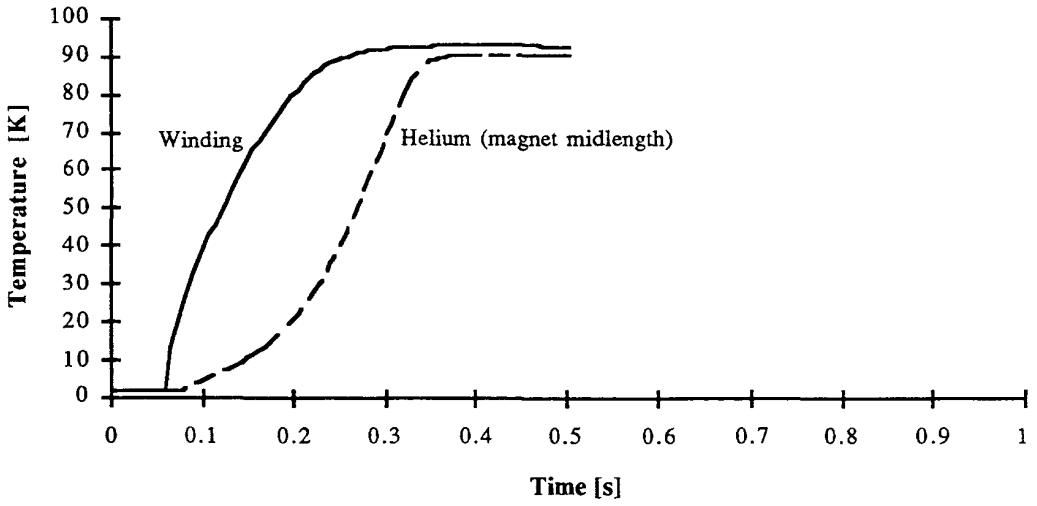

Figure 4.8 Winding and helium temperature

The winding temperature and the temperature of the helium in the annular space at magnet midlength is shown in figure 4.8. The maximum winding temperature is 93 K, reached after 0.4 s. The spatial distribution of the helium temperature along the annular is parabolic with the minimum temperature at magnet midlength.

D. Convective heat transfer coefficient, heat transfer area and multiplication factor

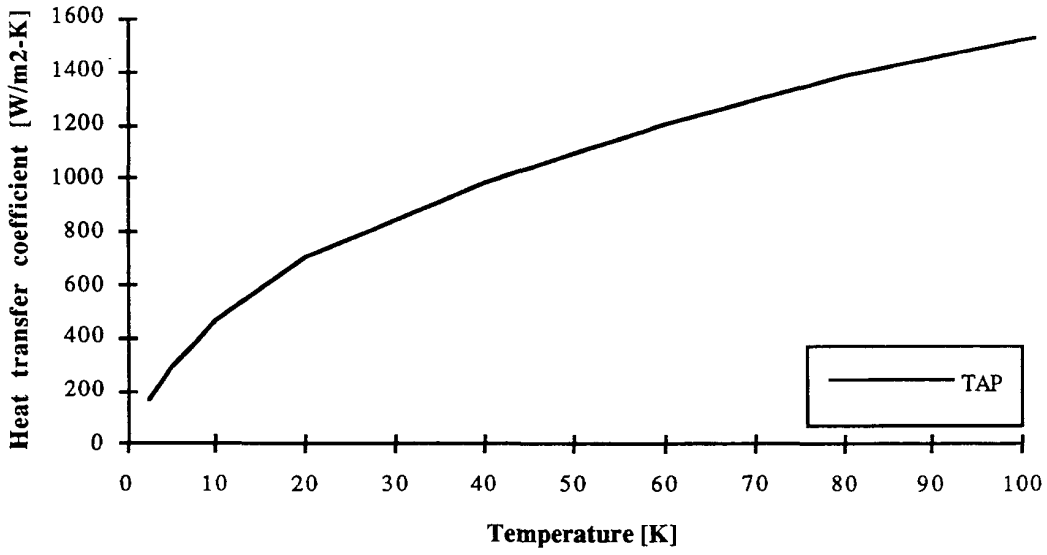

Figure 4.9 Convective heat transfer coefficient

The convective heat transfer coefficient between the winding and the helium in the annular space, calculated by equation (2.13), is shown in figure 4.9. The heat transfer area, the surface of the cylindrical aperture occupied by the superconducting cable, is 1.5 m^2. The multiplication factor 4.0 was used in the simulation.

E. Pressure transients with open relief valve

Figure 4.10 shows the simulated pressure transient in the annular space at magnet midlength and in each end reservoir. The corresponding measured pressures and the current decay are also plotted. The relief valve opens after 70 ms with an immediate opening. The simulated pressure transient in the annular space is well in accordance with the measurement.
The simulated pressure in the end reservoir next to the relief valve follows the evolution of the measured pressure up to 0.3 s, then they diverge. The simulated pressure in the end reservoir furthest away from the relief valve increases fast up to 16 bars after it decays slowly. The simulated pressure in each of the two end reservoirs shows completely different behaviour, which is not the case in the measurements where the pressures rises in the same way. The difference can be explained by the presence of a hydraulic connection between the end reservoirs, except the annular, which equilibrates the pressures. There are longitudinal holes in the yoke structure which can explain it.

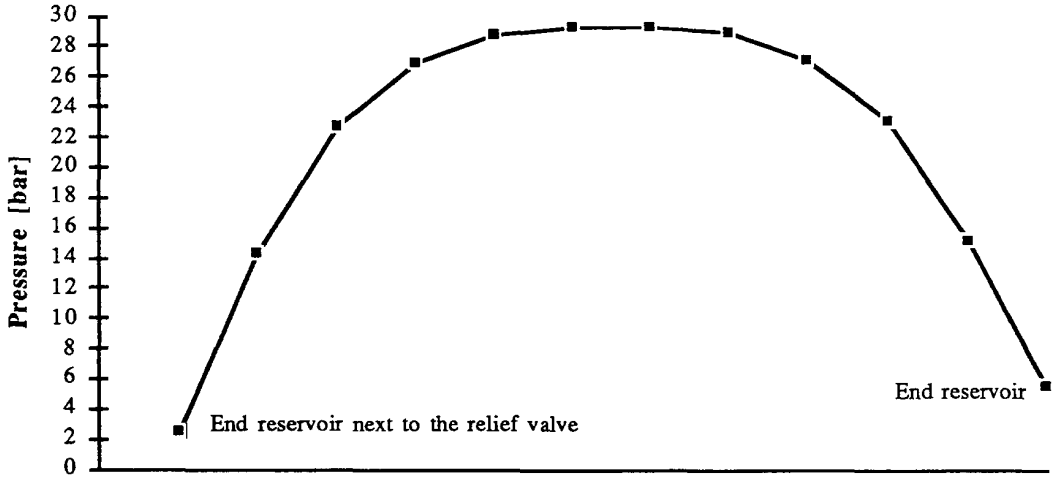

Figure 4.11 Spatial distribution of the pressure along the annular

The spatial distribution of the pressure along the annular at the time of the peak pressure is shown in figure 4.11. The pressure in each end reservoir is also shown. The peak pressure occurs at magnet midlength.

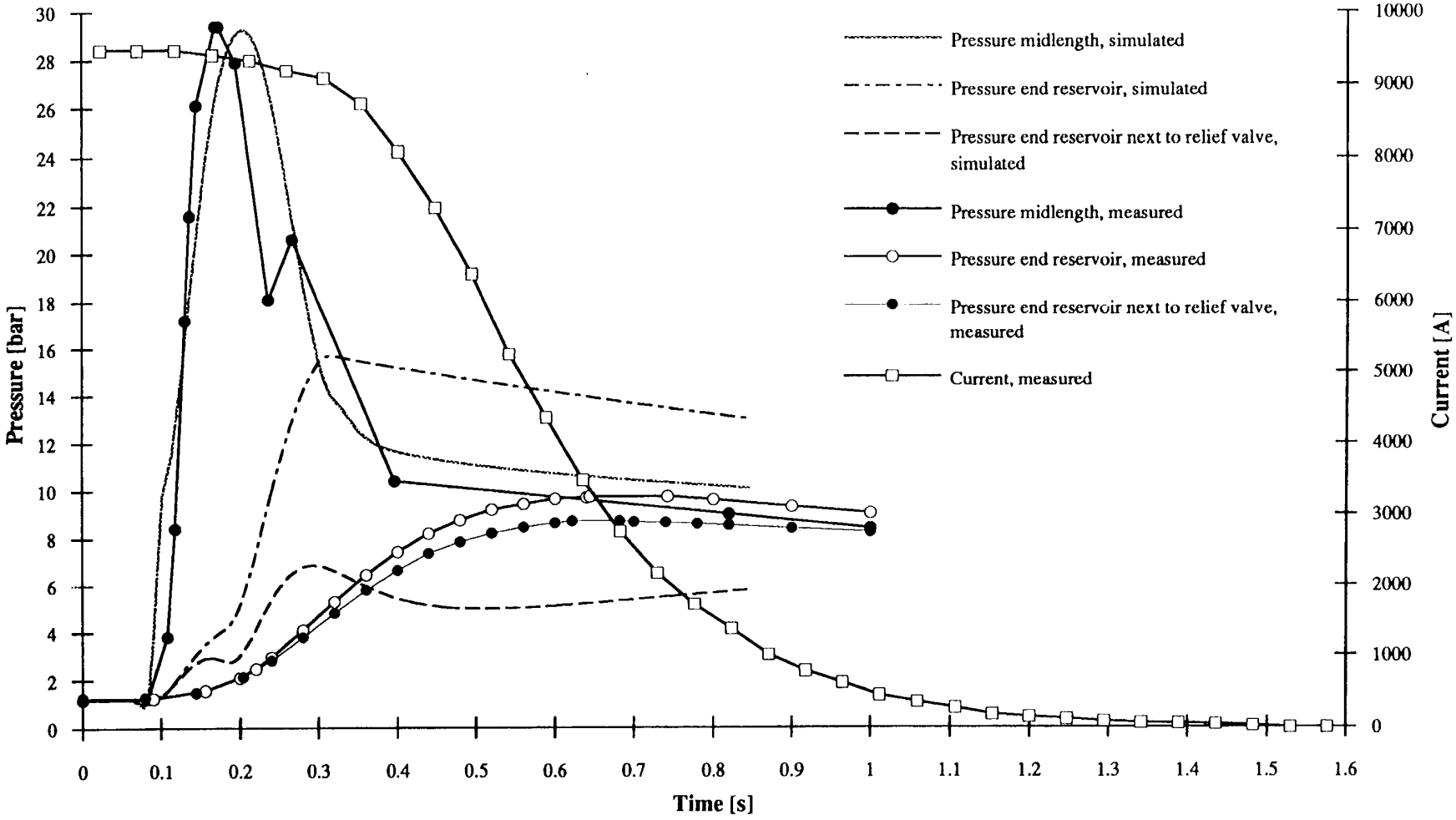

Figure 4.10 Measured and simulated pressure transients with open relief valve

F. Pressure transients with closed relief valve

The simulated pressure transient in annular space at magnet midlength and in each end reservoir with the relief valve remaining closed are shown in figure 4.12. It is observed here that the pressure at magnet midlength is independent on the opening of the relief valve. The pressure in each end reservoir is now identical, and shows both the same behaviour as the reservoir furthest away from the valve in the case of open relief valve (figure 4.10). The pressure in the cryostat helium vessel stabilises at about 17 bars after 0.35 s. The measured pressures, when the relief valve is open,g are also plotted for comparison.

G. Creation of the pressure transient in the annular space

It is of interest to study how the pressure transient in the annular space at magnet midlength is built up. The governing equation is the equation for conservation of momentum (2.1). The left side of the equation (2.1) represents the pressure drop due to acceleration and the right side expresses, in order; the total pressure drop, the pressure drop due to friction and the pressure drop due to abrupt change in cross-section. Figure 4.13 shows the pressure transient in the annular space at magnet midlength, separated into the different terms of pressure drop. The frictional pressure drop is the dominating term in the total pressure rise, with the exception of the beginning of the pressure rise, then the pressure drop is only due to acceleration of the fluid.

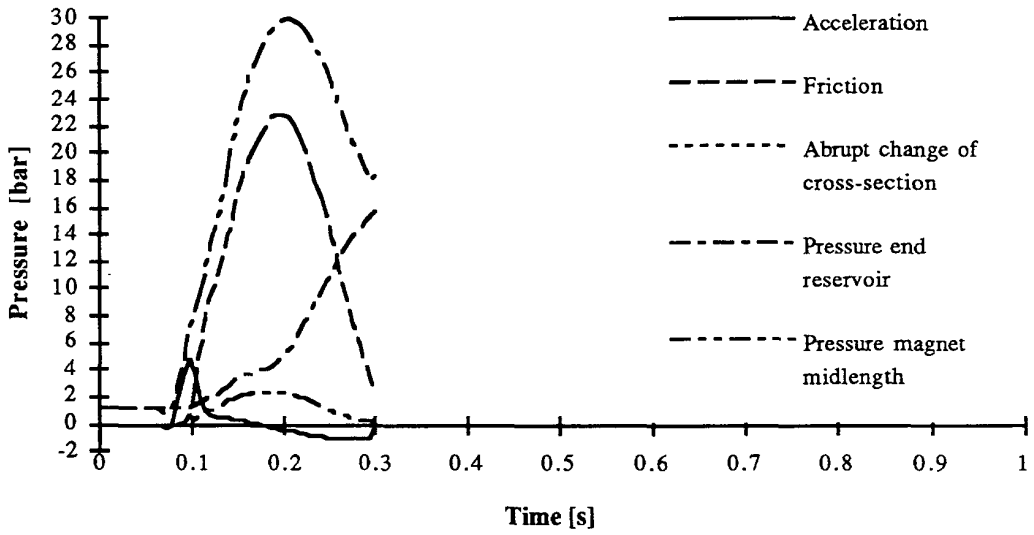

Figure 4.13 Pressure transient in the annular space at magnet midlength separated into different terms of pressure drop

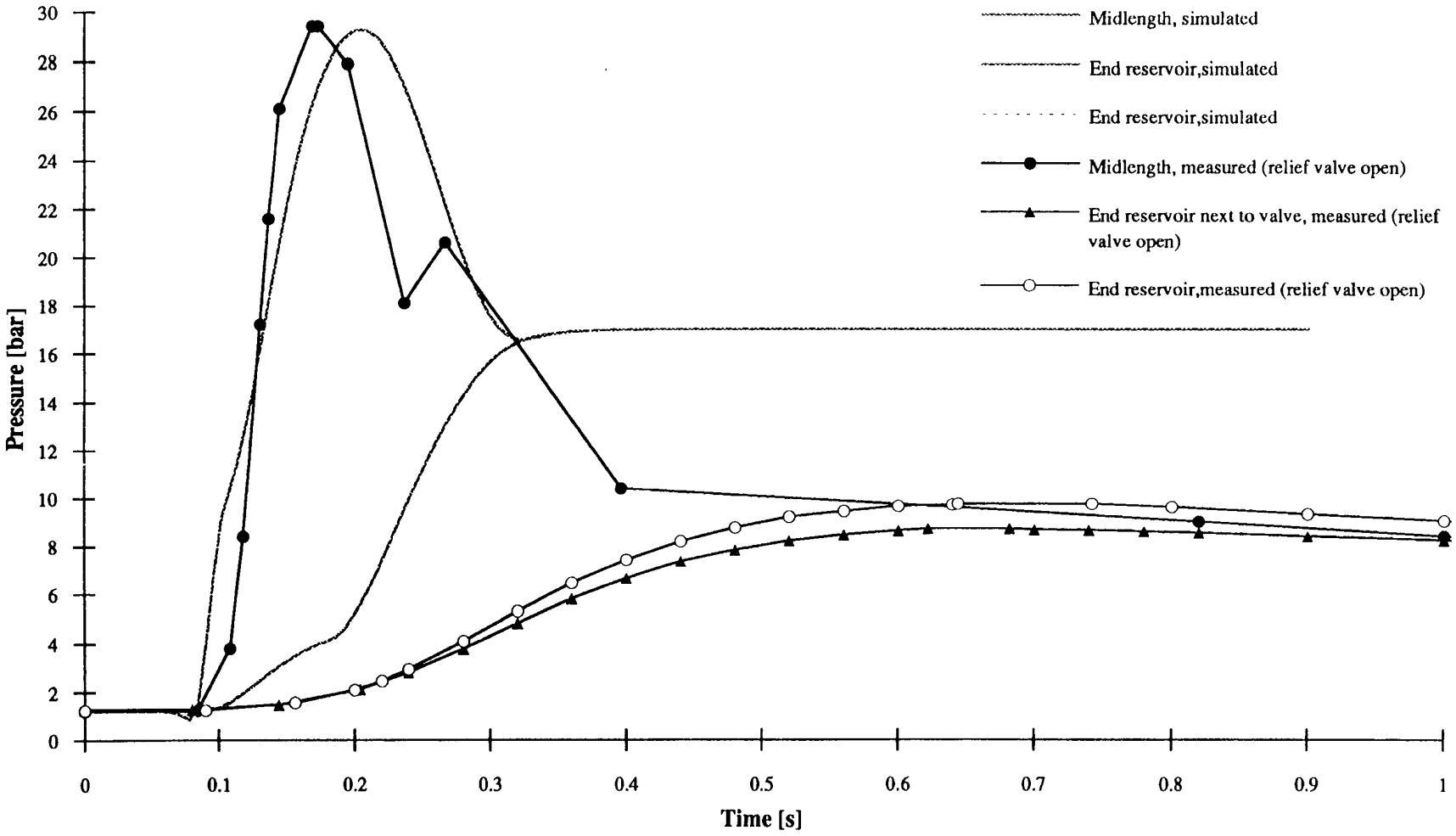

Figure 4.12 Simulated pressure transients with closed relief valve

H. Flow velocity and mass flow

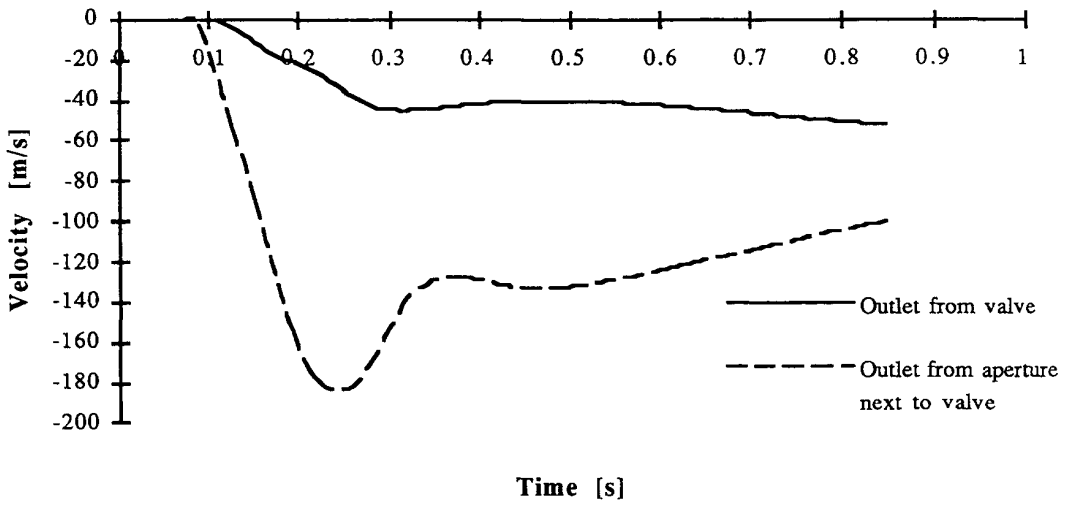

Figure 4.14 Flow velocity

The simulated flow velocity at the outlet of the aperture to end reservoir next to the relief valve and the velocity at the outlet of the relief pipe to constant pressure are shown in figure 4.14. The time of the maximum velocity at the outlet of the aperture coincide with the pressure peak at magnet midlength. The spatial velocity distribution in the annular at the time of peak pressure is shown in figure 4.15.

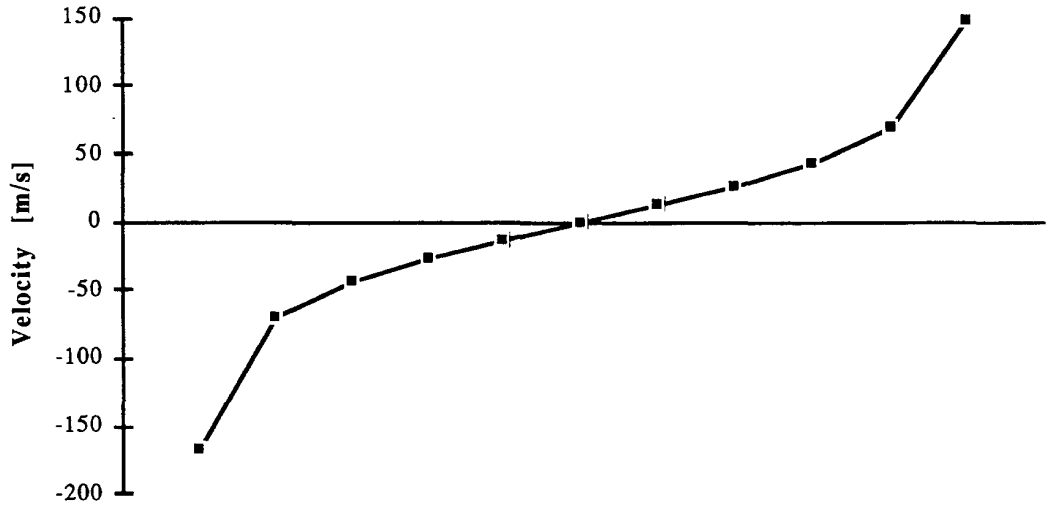

Figure 4.15 Spatial velocity distribution along the annular

The mass flow after the relief valve at the outlet of the relief pipe to constant pressure, figure 4.16, has the maximum absolute value 4.7 kg/s at 0.3 s. The corresponding measurement, figure 4.4, is 9 kg/s at 0.75 s. The magnitude of the simulated mass flow is well in agreement with the measurement, since it has to be multiplied by a factor of

two, due to only half the cross-section of the relief pipe being simulated (only one dipole is considered). The disagreement in time is difficult to explain. One explanation might be the lack of good hydraulic connection between the two end reservoirs in the simulation model. An accordance between the measured maximum end reservoir pressure and the measured maximum mass flow is observed. The same accordance is observed for the simulated pressure and mass flow.

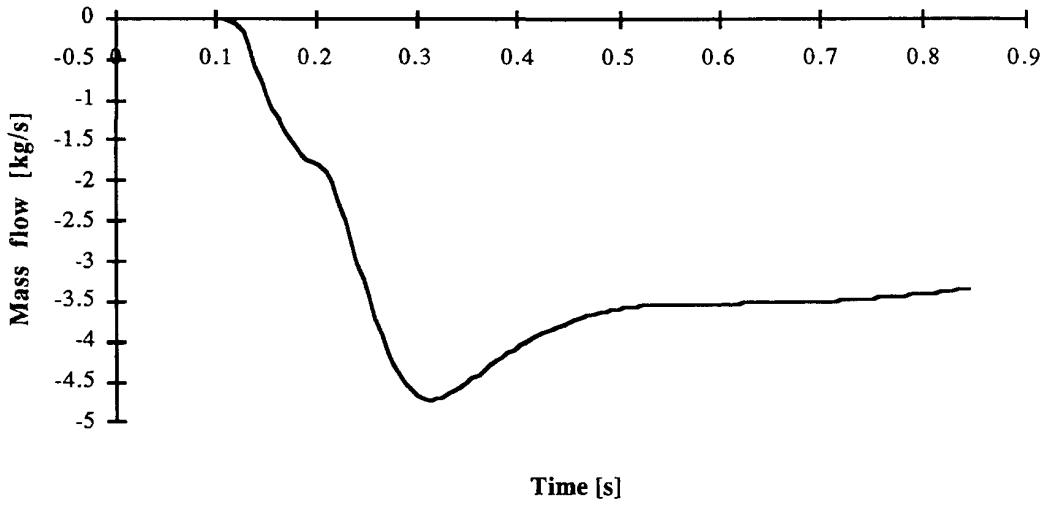

Figure 4.16 Mass flow after the relief valve

I. Helium density

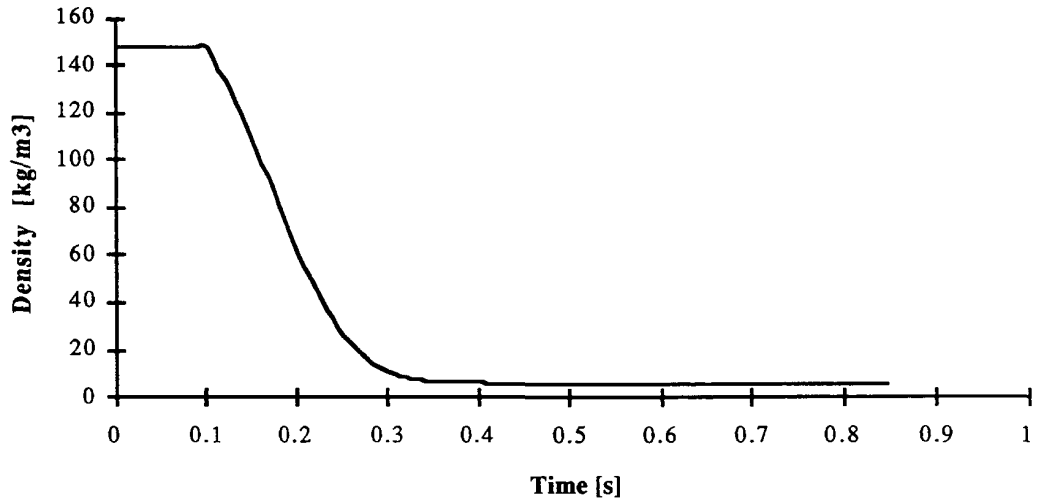

Figure 4.17 Density of the helium in the annular space at magnet midlength

The density of the helium in the annular space at magnet midlength is shown in figure 4.17. After about 0.3 s most of the helium in the annular has been expelled to the two end reservoirs. The spatial density distribution along the annular is parabolic with the maximum at magnet midlength.

J. Temperature of insulation, collars and yoke

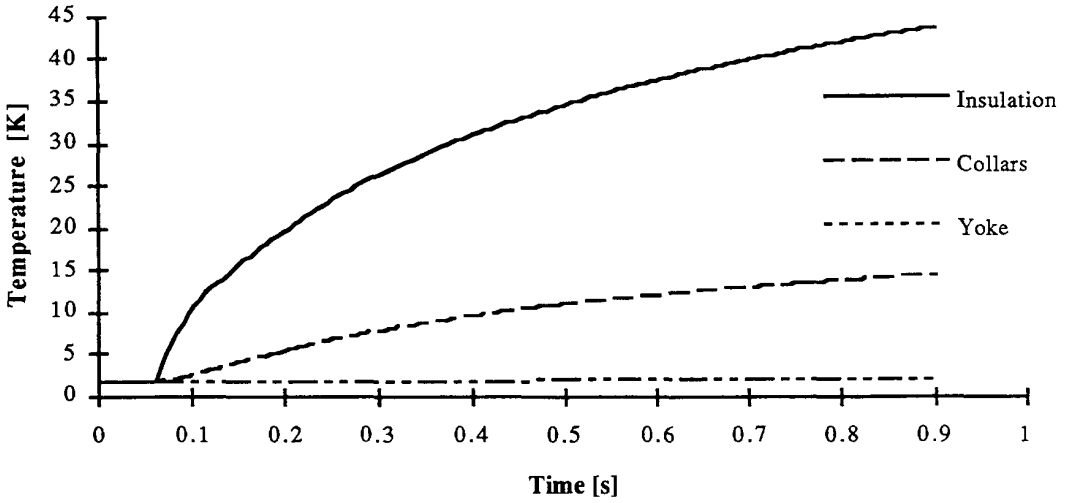

Figure 4.18 Temperature of insulation, collars and yoke

The simulated temperature of the insulation (between the winding and the collars), the collars and the yoke are shown in figure 4.18. The temperature of the insulation and the collars rise fast after the quench, in difference to yoke temperature which increases in the order of a few tenths of a degree, due to its large mass.

K. Friction factor

The friction factor at fully turbulent flow was 0.038, which is in accordance with measurements of the friction factor carried out on the short twin aperture dipole model.

L. Multiplication factor

The influence of the multiplication factor on the simulated peak pressure at different quench currents is shown in figure 4.19. The black marks indicate the chosen factors.With a multiplication factor of 3, the pressure peak in each of the four quenches can be simulated to within a 10% rate of accuracy. If the multiplication factor is increased the magnitude of the simulated pressure peak increases and the rise time becomes smaller.

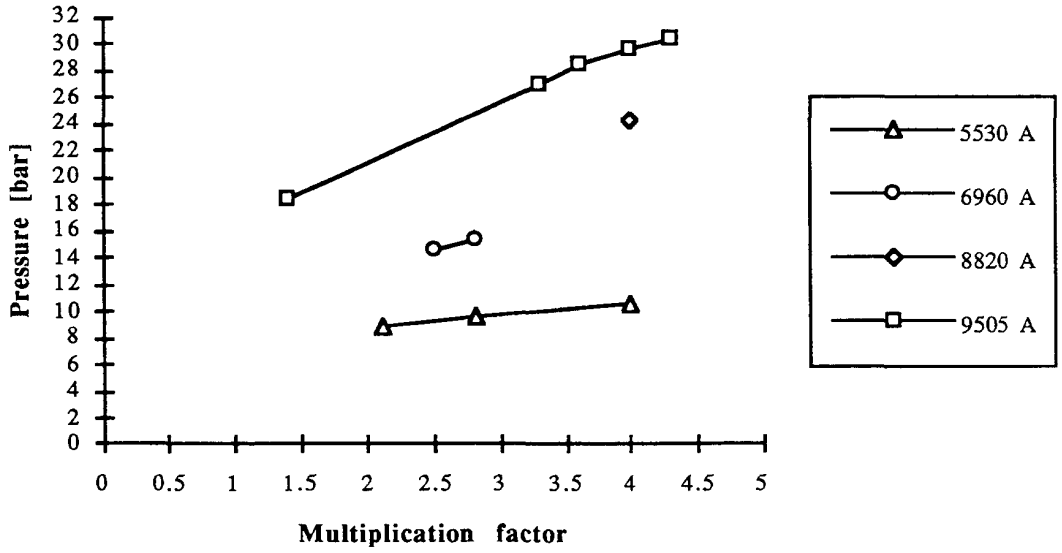

Figure 4.19 Peak pressure as function of the multiplication factor at different quench currents

M. Brief summary of simulation results

In table 4.3 a summary of the results from the simulated quenches is presented, where *Qdisp max* is the maximum power dissipated in the winding, *Qconv max* the maximum convected power from the winding to the helium in the annular space, *Twind max* the maximum winding temperature and *Pmax* the peak pressure .

Quench current [A]	*Qdisp max* [MW]	*Qconv max* [kW]	*Twind max* [K]	*Pmax* [bar]
5530	0.9	85	50	9
6960	3.5	174	65	17
8820	12.2	410	87	25
9505	16.0	480	93	29

Table 4.3 Summary of simulation results

4.1.4 Pressure transient dependence on annular space and magnet length

The simulated pressure peak as function of the magnet length and the annular space, scaled from a quench of the TAP magnet at 9505 A, are shown in figure 4.20 and 4.21 respectively.

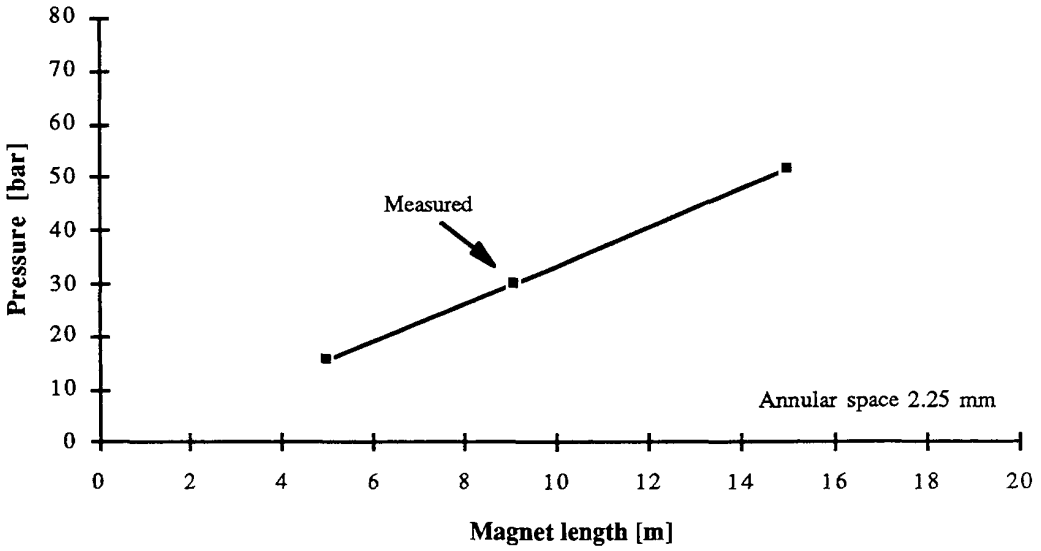

Figure 4.20 Peak pressure as function of magnet length, scaled from the TAP magnet

In figure 4.13 it was shown that the friction term is the dominating term in the total pressure rise. The governing relation of the frictional pressure drop, equation (2.2), shows that the frictional pressure drop increases in inverse proportion to the hydraulic diameter and proportionally to the magnet length and to the friction factor, which also can be seen in the figure 4.20.
A possible way to limit the peak pressure in long magnets is to reduce the effective flow length by adding radial venting channels connecting the annular space with the bulk volume of the helium vessel.

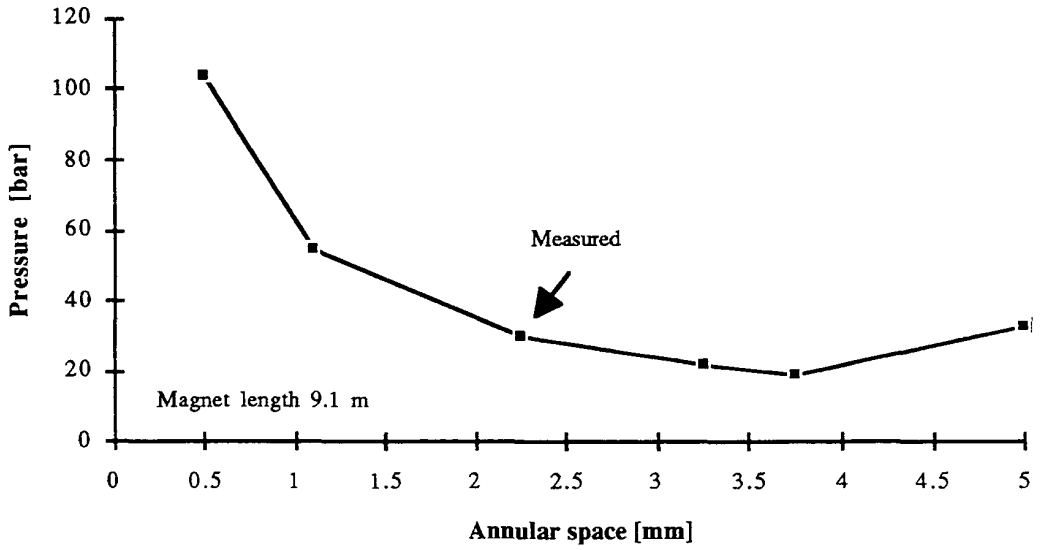

Figure 4.21 Peak pressure as function of annular space, scaled from the TAP magnet

In figure 4.21 it can be seen that the peak pressure as function of the annular space has a minimum. Then the annular space is smaller than in the minimum point, the peak pressure is governed by the frictional pressure drop and increases in inverse proportion to the annular space. For large annular space the frictional pressure drop is no longer the dominating term in the total pressure rise, since the friction factor and the flow velocity are small and the hydraulic diameter large, giving a uniform pressure rise in the whole magnet. The peak pressure can thus be limited by increasing the annular space around the beam tube up to a certain maximum value.

4.1.5 Conclusions

The maximum calculated power dissipation in the winding coincides in time with the measured peak pressure in the annular space around the beam tube. There is an apparent correlation, both in time and magnitude, between the peak pressure and the magnitude of the maximum power dissipation.

The simulations show that the frictional pressure drop is the dominating term in the total pressure rise in the annular space around the beam tube. The acceleration term only dominates at the beginning of the pressure rise.

The simulated pressure transient in the annular space is independent of the relief valve, i.e. if it is open or closed. The different behaviour in simulated and measured pressure transients in each of the reservoirs, then the relief valve is open, indicates that the two end reservoirs are well hydraulically coupled, which requires another hydraulic connection than the annular.
The peak pressure as a function of the annular space has a minimum. Then the annular space is smaller than in the minimum point, the peak pressure is governed by the frictional pressure drop and increases in inverse proportion to the annular space. For large annular space the frictional pressure drop is no longer the dominating term in the total pressure rise and there is no pressure drop along the annular, giving a uniform pressure rise in the whole magnet.

The peak pressure increases proportionally to the magnet length, and a way to limit the pressure peak in long magnets would be to limit their effective length by adding radial venting channels connecting the annular space around the beam tube with the bulk volume of the helium vessel.

4.2 SHORT TWIN APERTURE DIPOLE MODEL

4.2.1 Magnet data

A short twin aperture LHC dipole model [9] has been manufactured by ANSALDO GIE, Italy, and tested at CERN. The most important magnetic and geometric data are summarised in table 4.4.

Self inductance / dipole	2.6	mH
Magnetic length	1.21	m
Magnet diameter	0.577	m
Annular length	1.21	m
Aperture diameter	50	mm
Winding mass/dipole	32.6	kg
Winding mass inner layer/dipole	14.2	kg
Winding mass outer layer/dipole	18.4	kg

Table 4.4 Data of the short twin aperture dipole model

4.2.2 Measurements

The magnet has been equipped with instrumented beam tubes, lowered into a vertical cryostat and cooled to 1.8 K where a series of quenches at different excitation currents and under different rates of energy extraction have been provoked. Each of three stainless steel beam tubes, 1.26 m long with nominal external diameters 42.5 mm, 44.5 mm and 46 mm, were equipped internally with 3 capillaries of equal length and internal diameter 2.5 mm. Emerging radially these tubes are welded flush with the beam tube external surface at locations 275 mm, 630 mm and 990 mm from one end and communicate pressures developed around the beam tubes to Siemens KPY-14 absolute pressure sensors previously calibrated at 1.8 K.

Measurements from three quenches at the same excitation current, each with a beam tube with a different outer diameter inserted, have been studied, table 4.5.

D_{bt} [mm]	δ [mm]	I_o [A]	E_{magn} [kJ]
42.5	3.75	12000	187
44.5	2.75	12000	187
46	2	12000	187

Table 4.5 Quenches

D_{bt} is the outer beam tube diameter, δ the annular space, I_o the quench current and E_{magn} the stored energy in one dipole.

The measured pressure transients at magnet midlength, location 630 mm, are shown in figure 4.22. The peak pressure was measured 2.9 bars, 2.3 bars and 1.9 bars in order of increasing annular space. The rise time in all three quenches is 40 ms.

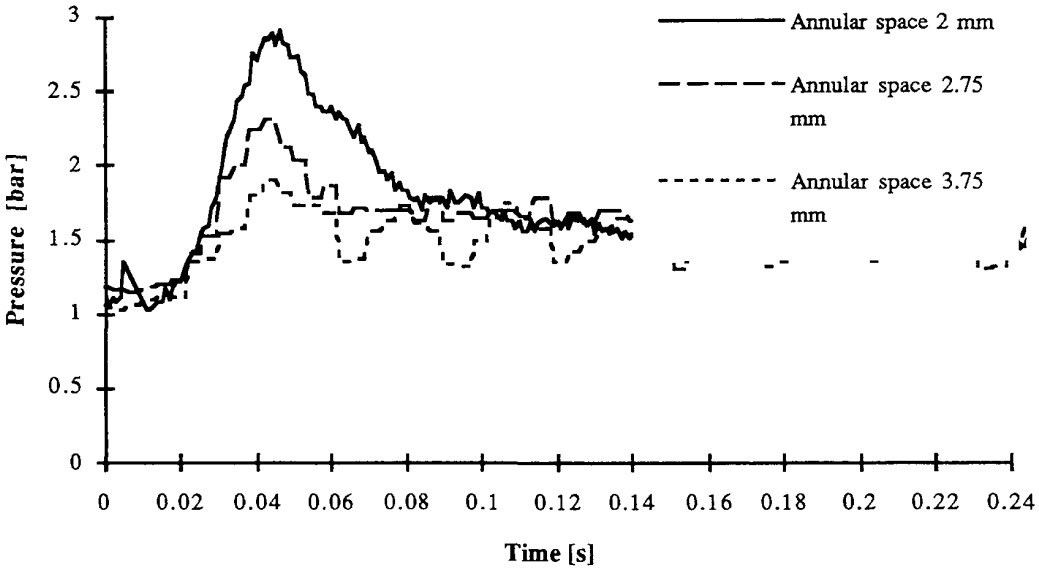

Figure 4.22 Measured pressure transients at magnet midlength for different annular space

In figure 4.23 the measured peak pressure as function of the annular space around the beam tube is shown.

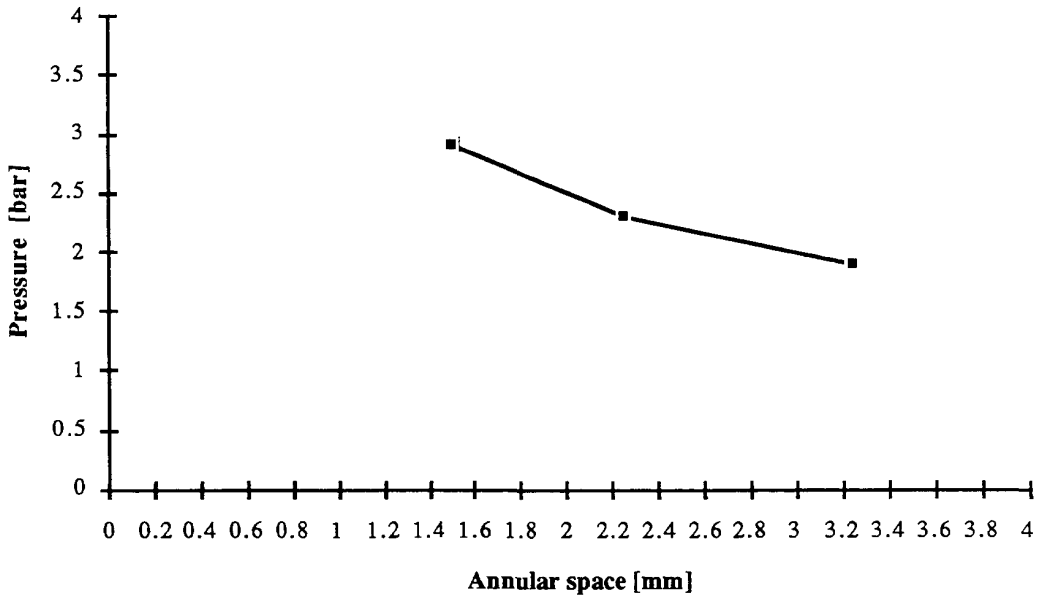

Figure 4.23 Measured peak pressure as function of annular space

4.2.3 Simulation results

Since the magnet is lowered into a vertical cryostat and immersed into helium, each end reservoir in the simulation model is assumed to contain a fourth of the cryostat helium content, i.e. 100 litres. The power dissipation in the dipole winding is assumed to occur only in the inner layer of the winding, since the measured rise time is too short to naturally quench both layers and the origin of a quench is normally at midplane of the inner layer.

A. Dissipation of energy in the winding

The power dissipation per dipole is calculated from equation (2.8) and is equal in all three quenches simulated, figure 4.24. The power dissipation reaches its maximum value 380 kW after 13 ms.

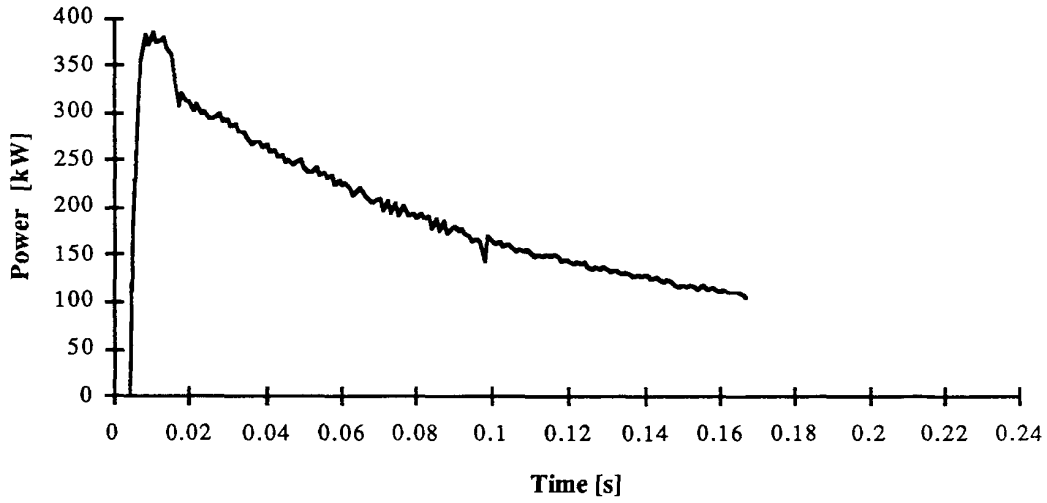

Figure 4.24 Calculated power dissipation per dipole

B. Convected power from the winding to the helium in the annular space and winding temperature

Table 4.6 shows the simulated power convected from the winding to the helium in the annular space around the beam tube and the temperature of the inner layer of the winding.

D_{bt} [mm]	d [mm]	Q_{conv} [kW]	T_{wind} [K]
42.5	3.75	15.5	≈40
44.5	2.75	14.4	≈40
46	2	13	≈40

Table 4.6 Simulated power convection and winding temperature

D_{bt} is the outer beam tube diameter, δ the annular space, Q_{conv} the convected power and T_{wind} the temperature of the inner layer of the winding.

C. Convective heat transfer coefficient, heat transfer area and multiplication factor

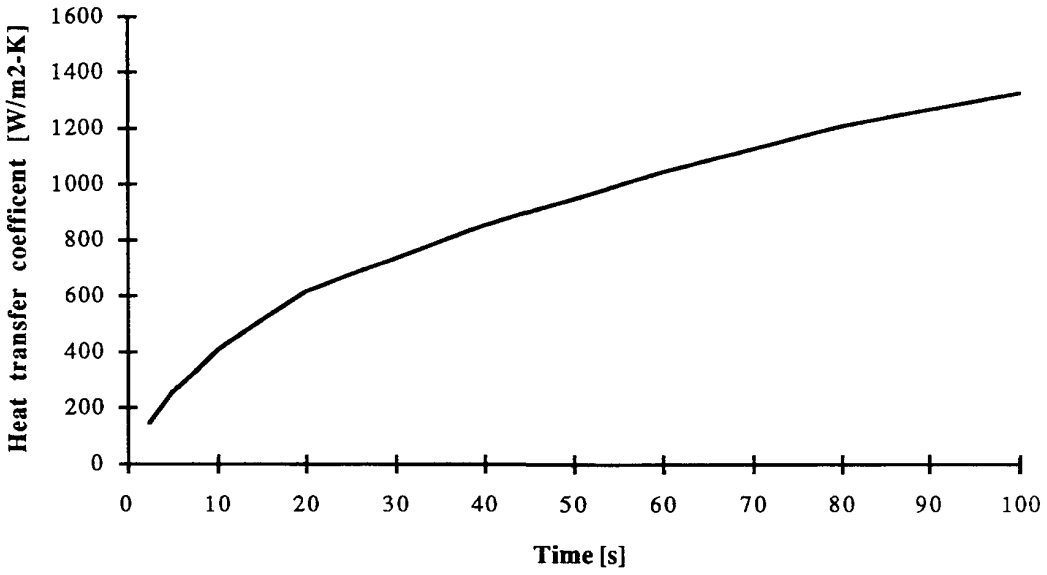

Figure 4.25 Convective heat transfer coefficient

The convective heat transfer coefficient between the winding and the helium in the annular space around the beam tube, used in the simulations of the short twin aperture model, is calculated by equation (2.13) and shown in figure 4.25. The heat transfer area, the surface of the cylindrical aperture occupied by the superconducting cable, is 0.11 m^2. The multiplication factor was 4.4 in all three simulations, and was determined with regards to the quench with the beam tube of 46 mm inserted.

D. Pressure transients

The pressure transient in the annular space around the beam tube at magnet midlength simulated for the three quenches listed in table 4.5, each with a beam tube of different outer diameter inserted, is shown in figure 4.26.
The simulated peak pressures in order of increasing annular space are 2.9 bars, 2.4 bars and 2.1 bars, which are slightly higher values than measured. The rise time is different in each simulation and are about a factor of two larger than measured. The first pressure bump is caused by acceleration of the helium and the same is observed in the simulations of the TAP dipole, but much less distinct. The large difference in rise time between the measured and the simulated pressure transient is probably due to the fact that the spatial propagation of the quench in the winding is not taken into account, which becomes important when the rise time is less than time required to quench the whole winding.

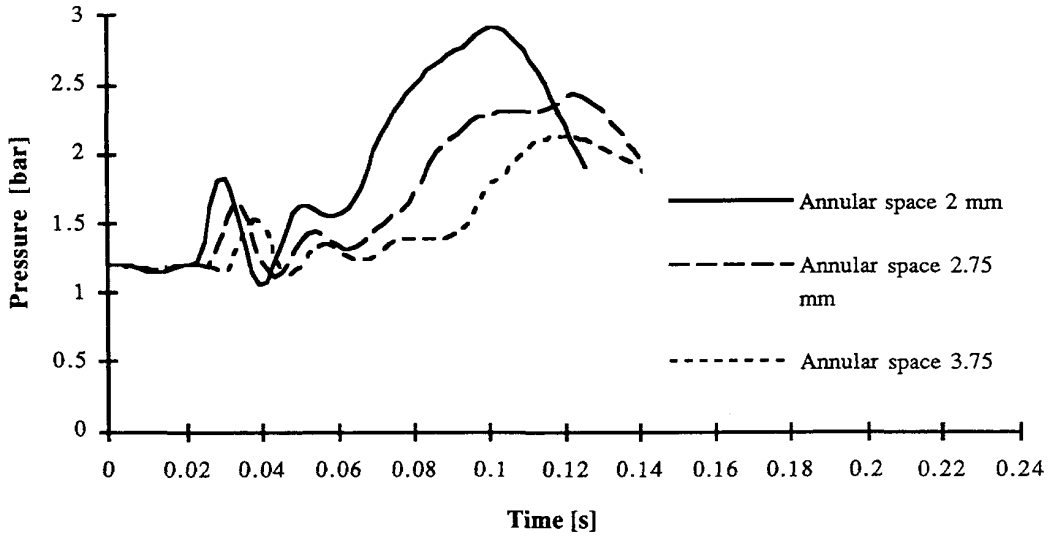

Figure 4.26 Simulated pressure transient in the annular space at magnet midlength for different annular space

4.2.4 Conclusions

One of the aims of the measurements on this short twin aperture LHC dipole model was to justify the effect of the annular space around the beam tube on the peak pressure. The measured peak pressure as a function of the annular space shows, for the same range of the annular space, the same characteristic curve as simulated on the TAP magnet (figure 4.21 and 4.23)

4.3 THE INFN PROTOTYPE

4.3.1 Magnet data

The INFN prototype (Instituto Nazionale di Fisica Nucleare) is a quasi-full scale twin aperture LHC dipole, designed and tested by CERN and manufactured by ANSALDO GIE, Italy. The prototype concerned is the second from ANSALDO GIE, called INFN 2. The most important magnetic and geometric data are summarised in table 4.7.

Self inductance / dipole	28.5	mH
Magnetic length	9.672	m
Magnet diameter	0.559	m
Annular length	9.672	m
Aperture diameter	50	mm
Beam tube outer diameter	45.5	mm
Annular space	2.25	mm
Winding mass/dipole	425	kg
Winding mass inner layer/dipole	218	kg
Winding mass outer layer/dipole	207	kg
Helium volume in annular space	3.2	litres
Helium volume reservoirs/magnet	83.6	litres

Table 4.7 INFN 2 magnet data

4.3.2 Measurements

One of the apertures of the magnet has been equipped with three probes for pressure measurement, located at magnet midlength and at a quarterly intervals from each end of the magnet length. The pressure in each end reservoir was also measured. Measurements at a series of natural quenches at different excitation currents have been carried out. The results from one of the high current quenches are presented here. The quench current was 13402 A giving the stored energy per dipole 2.55 MJ and the magnetic field 9.04 T. The helium bath temperature was 1.63 K.

In figure 4.27 the measured pressure transients and the current decay during the quench is shown. The funnel side is the side of the magnet next to the relief valve and the MM side the other side furthest away, figure 2.1. The peak pressure is 11.3 bars after 0.3 s and the rise time is 124 ms. The three pressures evolve in the same way, which is different from what is observed on the TAP magnet. The reason is probably better hydraulic connection between the annular space around the beam tube and the two end reservoirs, due to radial venting through the collars and the yoke, which is discussed in §4.4. It has been observed that the pressure transients start to decay when the relief valve is fully open.

The measured mass flow after the relief valve is shown in figure 4.28.

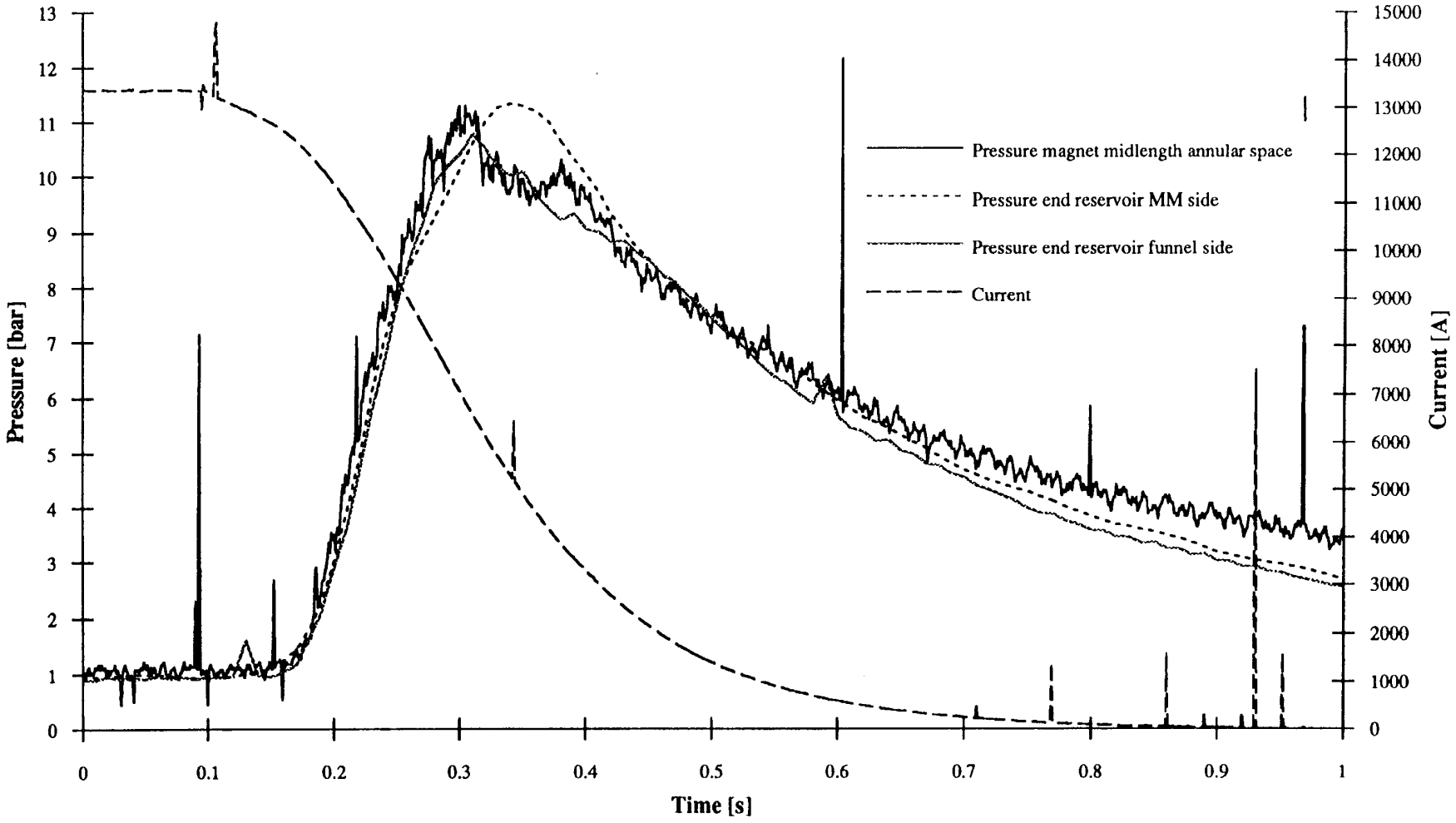

Figure 4.27 Measured pressure transients and current

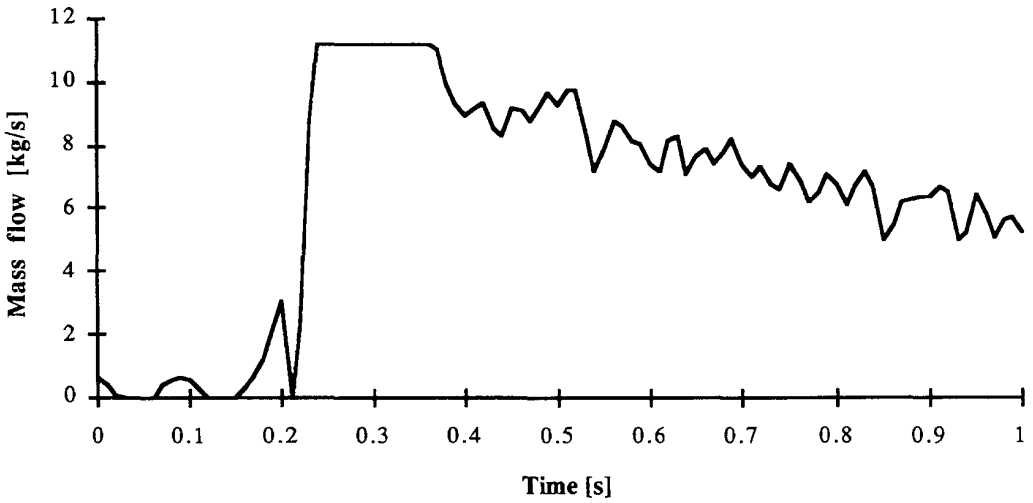

Figure 4.28 Mass flow measured after the relief valve

4.3.3 Simulation results

The results from the simulation of the quench at excitation current 13402 A in the INFN 2 magnet will here be presented.
Only the inner layer of the winding is considered in the simulation model, since the dimensions of the cable in the two layers are different, giving rise to different power dissipation and temperature between the two layers.

A. Power dissipation in the winding

The growth of the resistance in the dipole winding during the quench, separated into layers and poles, is shown in figure 4.29. The resistance is calculated from equation (2.8). It should be noted here the large difference in resistance between the outer and inner layers.

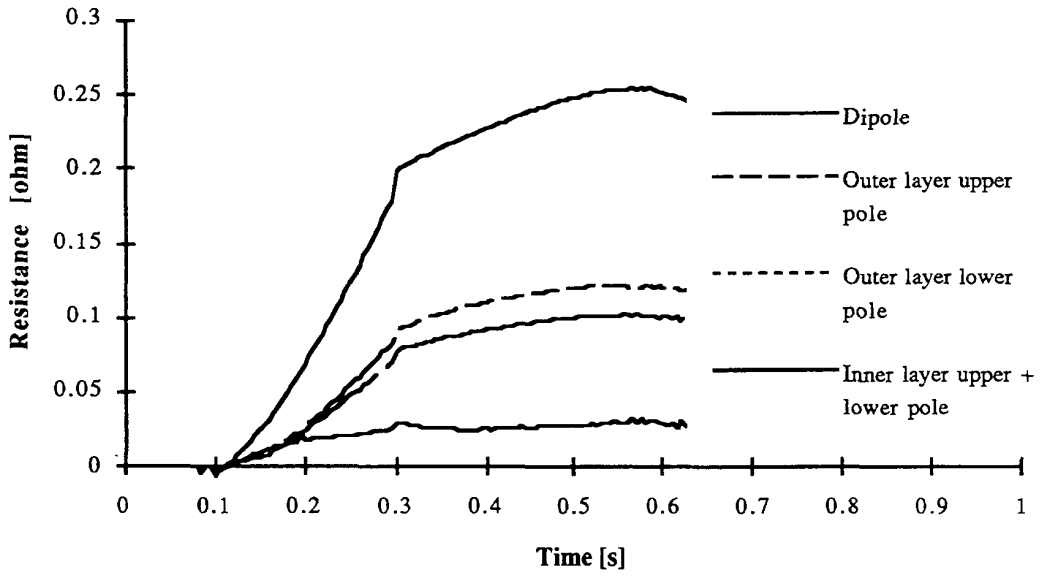

Figure 4.29 Winding resistance

The power dissipation is calculated per layer and pole from equation (2.9), see figure 4.30. Since the resistance is significantly different in the two layers of the winding, the power dissipation shows the same difference. The maximum dissipation in the inner layer is 2.3 MW after 0.20 s and in the whole dipole 10.9 MW after 0.25 s. It can also be observed here, as for the TAP magnet, that the peak pressure occurs at about the same time as the maximum power dissipation in the winding.

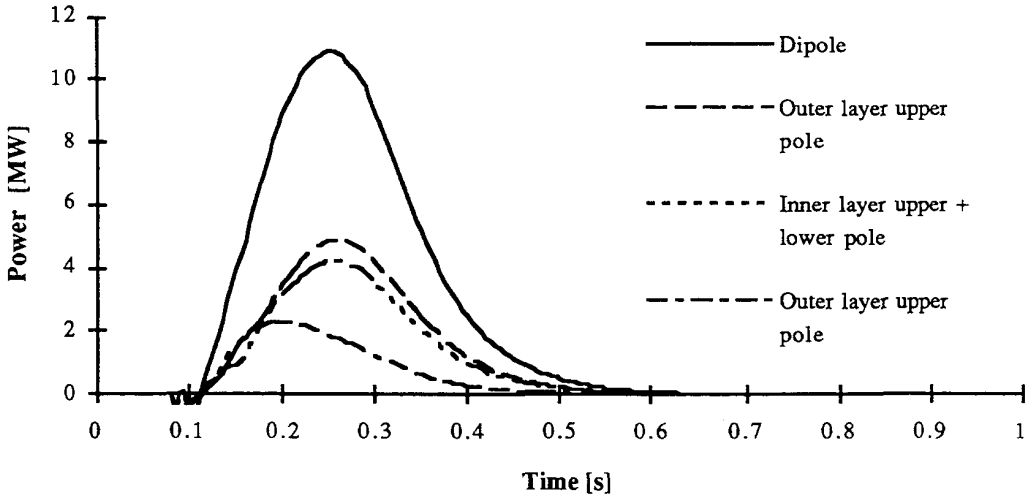

Figure 4.30 Power dissipation in the winding

B. Power transferred from the winding to the helium in the annular space around the beam tube

The total power convected along the annular from the inner layer of the winding to the helium in the annular space around the beam tube, governed by equation (2.6), is shown in figure 4.31. The maximum power convected is 66 kW at 0.34 s, and the spatial distribution along the annular is parabolic with the maximum at magnet midlength.

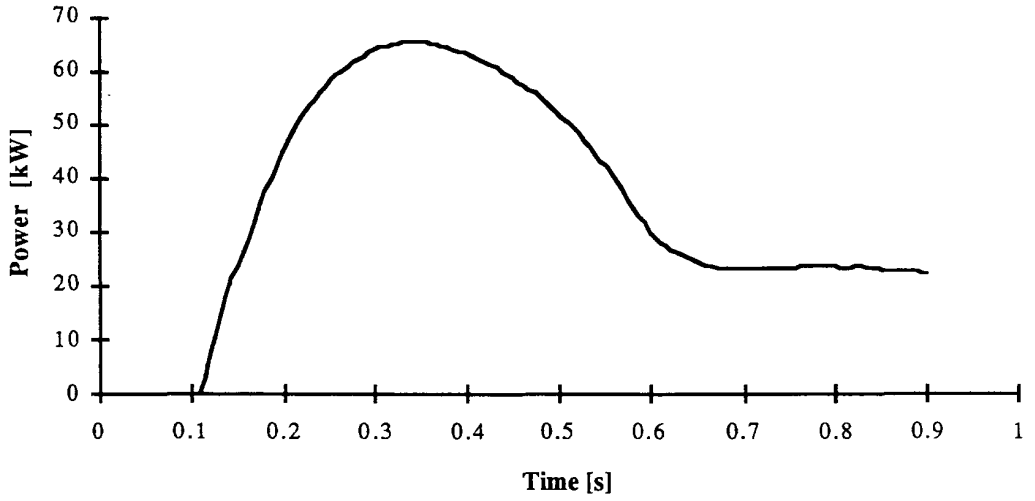

Figure 4.31 Total convected power from the inner layer of the winding to the helium in the annular space

C. Winding and helium temperature

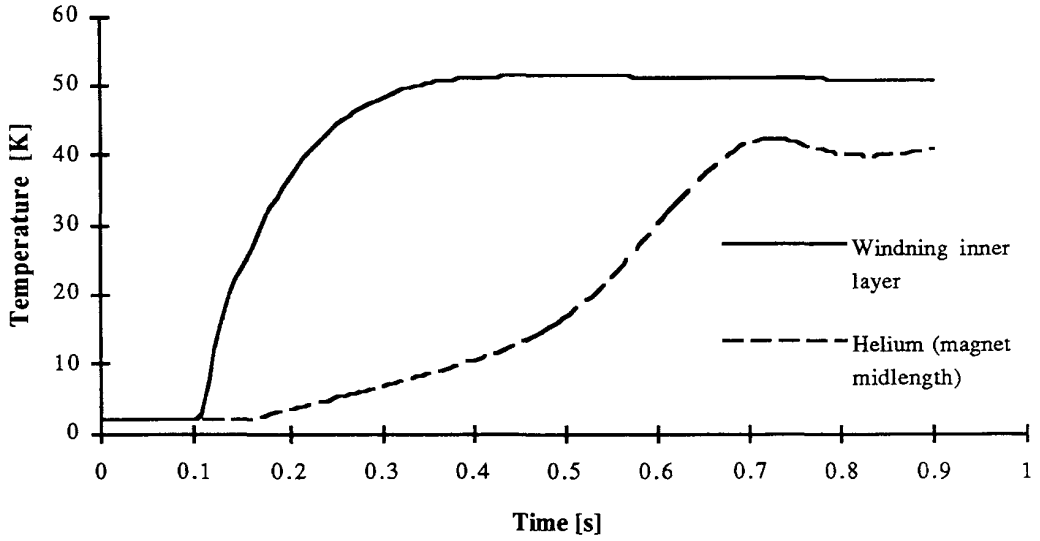

Figure 4.32 Temperature of the inner layer of the winding and of the helium in the annular space at magnet midlength

The temperature of the inner layer of the winding and of the helium in the annular space at magnet midlength is shown in figure 4.32. The maximum winding temperature is 51 K, reached after 0.4 s, and the spatial distribution of the helium temperature along the annular is parabolic with the minimum temperature at magnet midlength.

D. Convective heat transfer coefficient, heat transfer area and multiplication factor

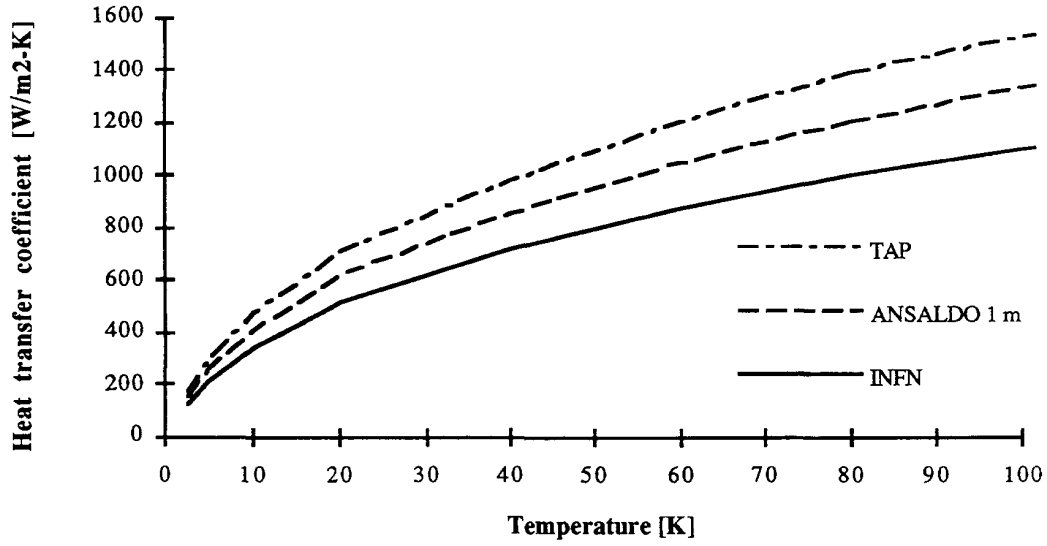

Figure 4.33 Convective heat transfer coefficient

The convective heat transfer coefficient between the winding and the helium in the annular space, used in the simulations of the INFN 2 magnet, calculated by equation

(2.13), is shown in figure 4.33. The heat transfer coefficient used in the simulation of the two other magnets are shown for comparison. The heat transfer area, the surface of the cylindrical aperture occupied by the superconducting cable, is 1.3 m^2, and the multiplication factor was 1.5.

E. Pressure transients with open relief valve

Figure 4.34 shows the measured and simulated pressure transients in the annular space at magnet midlength and the simulated pressure rise in each end reservoir. The relief valve is initially open in the simulation, while in the measurement it is fully open after about 0.3 s. The simulated pressure peak agrees with the measurement, but the pressure rise in each end reservoir shows a completely different behaviour than the measurements, a behaviour similar to the simulation on the TAP magnet. The reason for this deviation between the simulation and the measurements is probably due to radial venting from the annular space through the collars and the yoke is neglected in the model.
It has been observed from the measurements that the measured pressure transient in the annular space at magnet midlength starts to decay when the relief valve becomes fully open, which is not the reason for the decay of the simulated pressure transient.

F. Pressure transients with closed relief valve

The simulated pressure transient in the annular space at magnet midlength and in each end reservoir with the relief valve remaining closed are shown in figure 4.35. The measured pressure transient in the annular space is also plotted for comparison. The simulated pressure transient in the annular space is in order of 1 bar larger than in the simulation with the relief valve being open, and the pressure rise in both the end reservoirs are now identical. The pressure in the cryostat helium vessel stabilises at 10.5 bars after about 0.9 s.

G. Flow velocity and mass flow

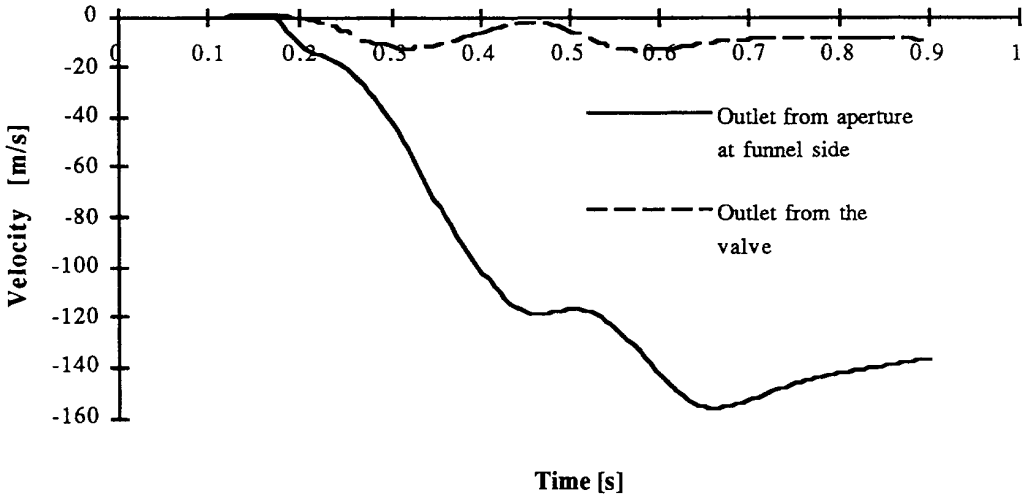

Figure 4.36 Flow velocity

The simulated flow velocity at the outlet of the aperture at the funnel side and at the outlet from the relief valve are shown in figure 4.36.

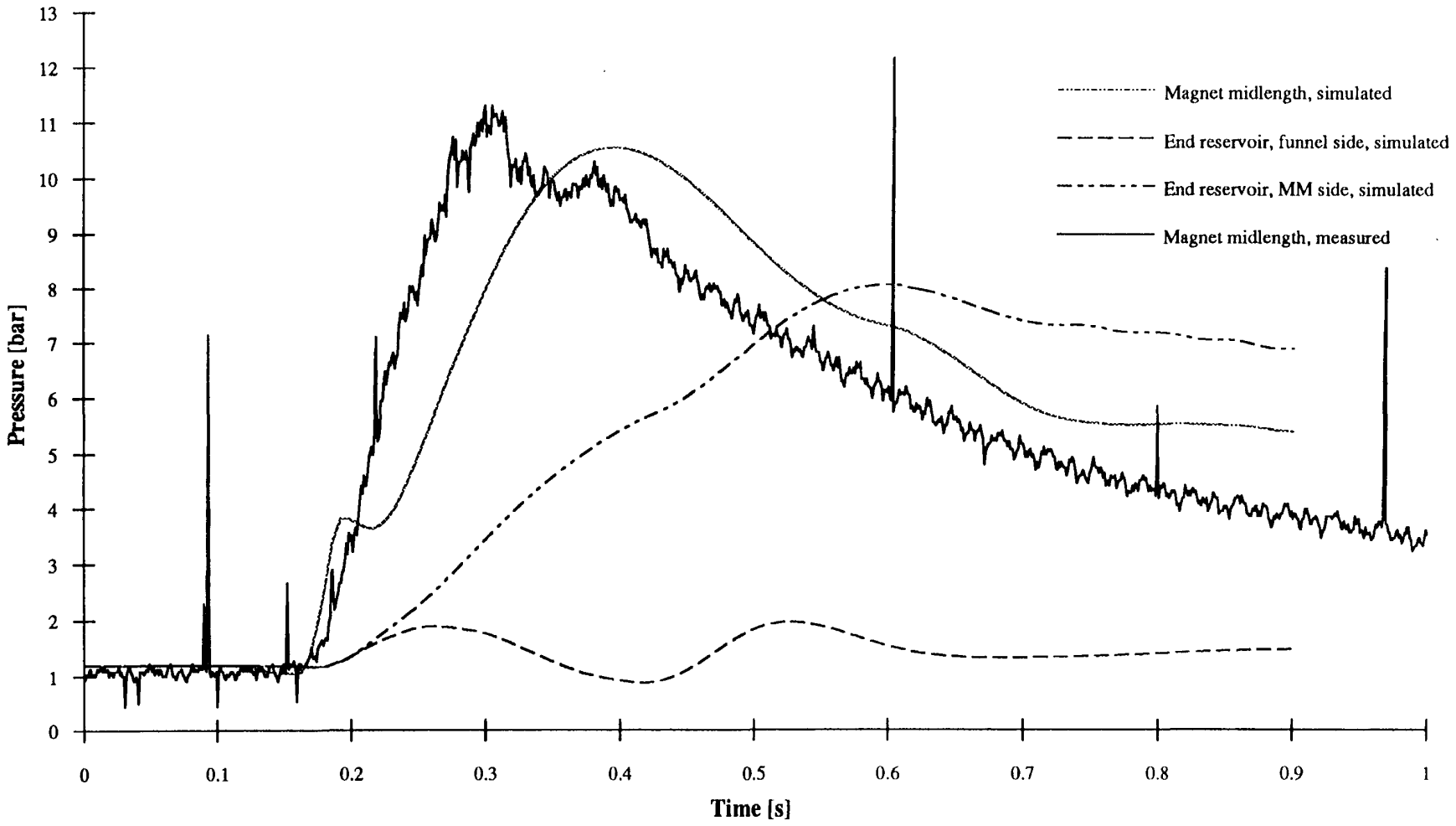

Figure 4.34 Measured and simulated pressure transients with open relief valve

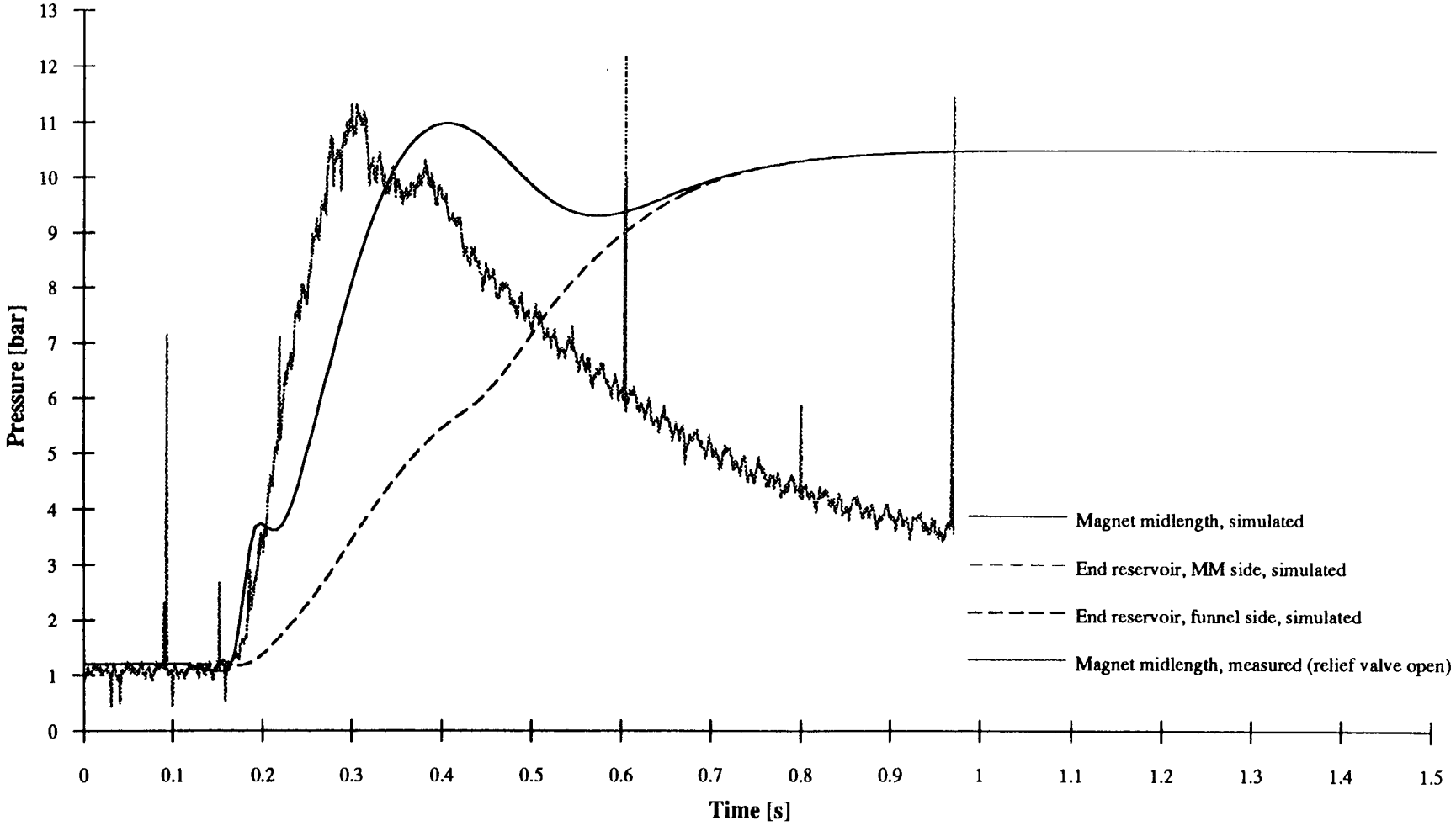

Figure 4.35 Simulated pressure transients with closed relief valve

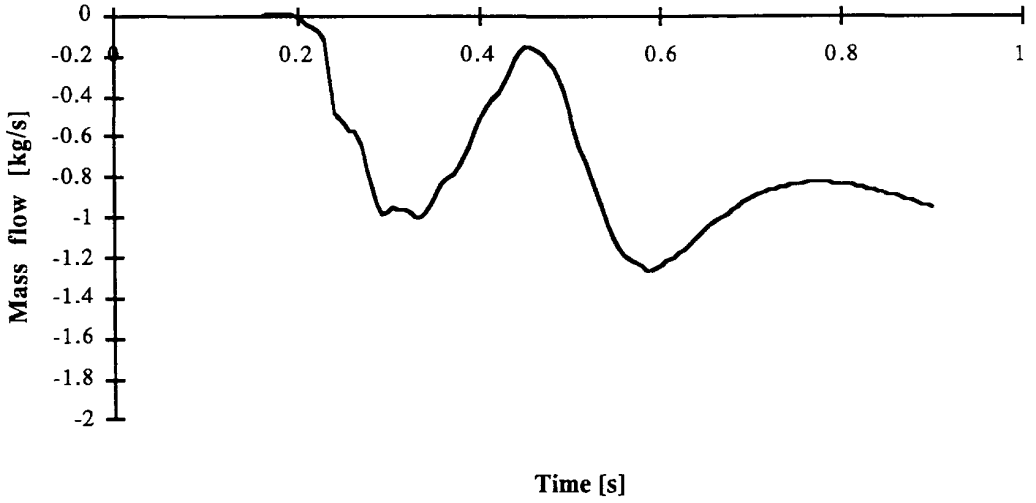

Figure 4.37 Mass flow after the relief valve

The simulated mass flow after the relief valve, figure 4.37, is not in accordance with the measurement.

H. Helium density

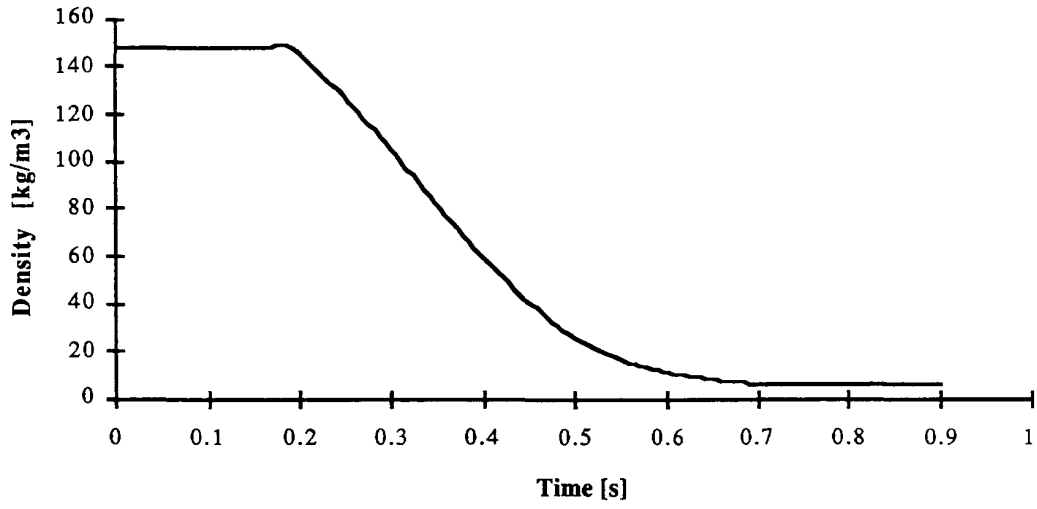

Figure 4.38 Helium density in the annular space at magnet midlength

The density of the helium in the annular space at magnet midlength is shown in figure 4.38. After about 0.6 s most of the helium in the annular has been expelled to the two end reservoirs. The spatial density distribution along the annular is parabolic with the maximum at magnet midlength.

I. Temperature of insulation, collars and yoke

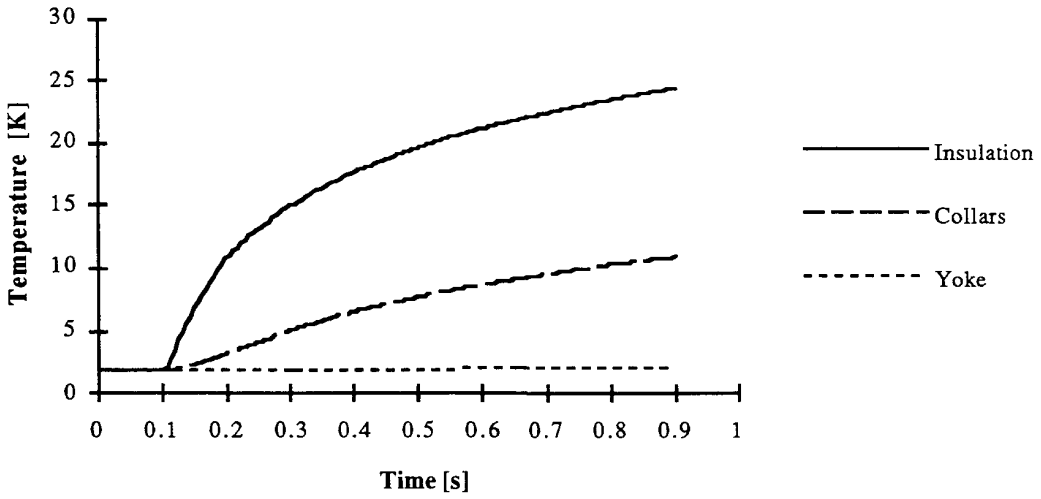

Figure 4.39 Temperature of insulation, collars and yoke

The simulated temperature of the insulation (between the winding and the collars), the collars and the yoke are shown in figure 4.39. The yoke temperature rises only a few tenths of a degree.

J. Friction factor

The friction factor at fully turbulent flow was 0.038, which is in accordance with measurements of the friction factor carried out on the short twin aperture dipole model.

4.3.4 Pressure transient dependence on annular space and magnet length

The simulated peak pressure as function of the annular space around the beam tube and the magnet length, scaled from the quench at current 13402 A, are shown in figure 4.40 and 4.41 respectively. The simulations were performed with the relief valve closed.

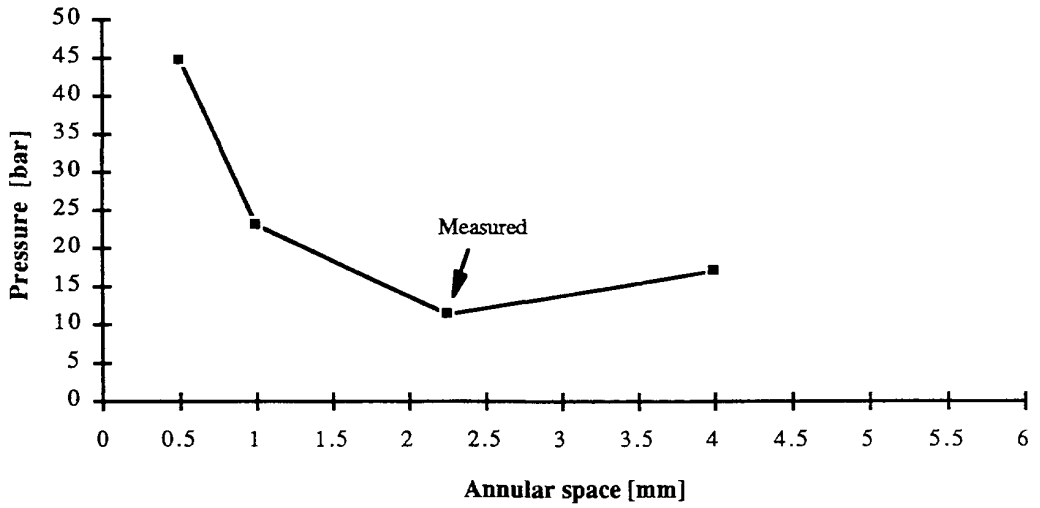

Figure 4.40 Peak pressure as function of the annular space around the beam tube

The peak pressure as function of the annular space around the beam tube shows the same characteristic curve with a minimum, as simulated on the TAP magnet.

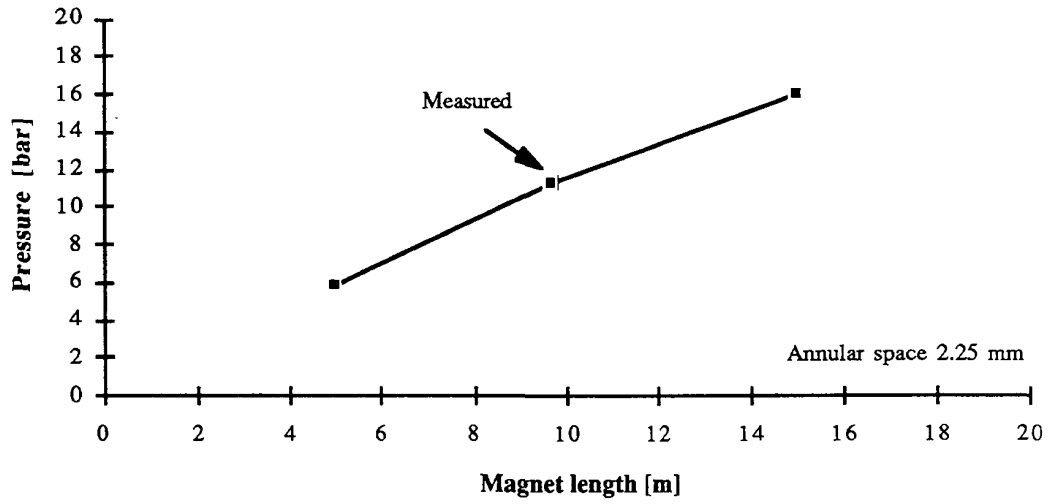

Figure 4.41 Peak pressure as function of the magnet length

The simulated peak pressure as function of the magnet length increases proportionally to the magnet length, as the simulations on the TAP magnet also showed.

4.3.5 Conclusions

The simulation model does not represent the physics behind the pressure transients in the INFN 2 dipole due to quench. The simulated pressure rise in the annular space around the beam tube is in accordance with the measurement, but measurements indicate that the pressure starts to decrease when the relief valve becomes fully open, which is not the case in the simulation, where the evolution of the pressure is unaffected with the relief valve being closed.
The reason for the decrease of the measured pressure in the annular space due to fully open relief valve is the uniform pressure rise of the whole magnet, which is not the case in the simulations, where there is a pressure drop along the annular (mainly due to friction) giving the pressure peak and separating the pressure peak from the pressure in each end reservoir.

The uniform pressure rise in the magnet is probably due to the venting of helium from the annular space radially through the laminated collars and yoke, followed by longitudinal venting through holes in the yoke structure to both the end reservoirs. The simulation model does not include the possibility of radial venting. The helium content, particulary in between the laminations of the collars, probably also vents to both the end reservoirs, pushed by the gaseous helium vented from the annular space.

There are obviously differences in magnet design between the TAP and the INFN 2 magnet, allowing radial venting in the latter magnet. The differences are positive from the point of view of quench pressure transients, and some of the design differences are discussed in §4.4.

4.4 DIFFERENCES IN MAGNET DESIGN

The measurements and simulations of the TAP and the INFN 2 magnet indicate differences in design. Radial venting of helium from the annular space around the beam tube seems to occur during quench in the INFN 2 magnet but not in the TAP magnet. Some design differences will here be discussed which can explain the differences.

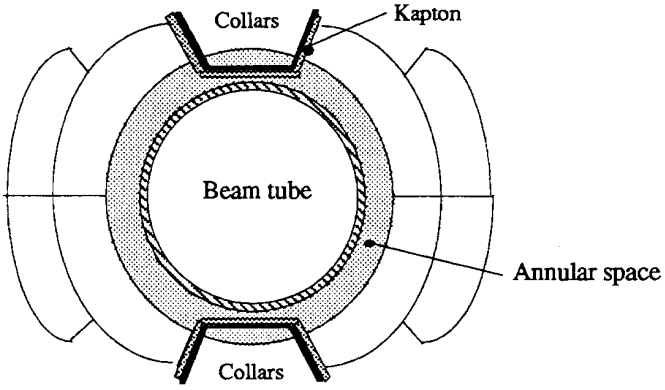

Figure 4.42 Aperture of the TAP magnet

Figure 4.42 shows how the nose of the collar laminations extends into the annular space around the beam tube in the TAP magnet. The nose is covered by a Kapton layer, obstructing the venting of helium radially through the collar laminations. In the INFN 2 magnet no material covers the nose.

The collar laminations in the INFN 2 magnet are separated by 0.050 mm thick Kapton washers, in contrast to the TAP magnet, where the collar laminations are stacked next to each other without washers.

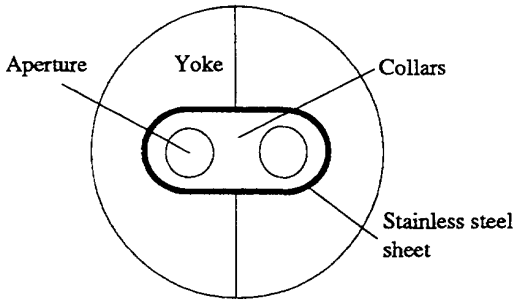

Figure 4.43 Cross-section of the TAP magnet

Figure 4.43 shows a simplification of the TAP magnet cross-section. The outer surface of the collar package is covered by a stainless steel sheet blocking radial flow of helium from the collars to the yoke.

These differences in magnet design can explain that radial venting of helium from the annular space around the beam tube through the collar and yoke laminations is possible in the INFN 2 magnet and not in the TAP magnet.

5. CONCLUSIONS

A study of the evolution of pressure transients in prototypes of the LHC superconducting dipoles due to resistive transition (quench) has been presented. The main objectives of the study were to achieve a further understanding of the physics behind the fast pressure peak in the annular space around the beam tube at magnet midlength and to analyse the effect of the magnet length, and the beam tube diameter on the pressure peak. The main conclusions of the study will be discussed here.

The evolution of the pressure transient in the annular space is first of all associated to the power transferred from the resistive winding to the helium in the annular space, and the transferred power is dependent on the power dissipated in the winding. The magnitude of the pressure peak cannot be predicted from the energy stored in the dipole.

The simulations show that the frictional pressure drop is the dominating term in the total pressure rise in the annular space around the beam tube, except at the beginning of the pressure rise up to a few bars and then the pressure is caused only by acceleration. The magnitude of the acceleration term is almost unaffected when the annular space becomes small.

The simulation of the TAP magnet showed that the pressure transient in the annular space is not dependent on the relief valve being open or closed. In the simulation the opening of the relief valve reduces the pressure rise only in the end reservoir next to the valve and the pressure in the other reservoir remains unaffected, in contrast to the measurements where the pressure in the two end reservoirs develop in the same way. This indicates that the two end reservoirs are in reality hydraulically well coupled, probably by longitudinal holes in the yoke structure.

The simulations show that the peak pressure in the annular space increases proportionally to the magnet length, and a way to limit the pressure peak in long magnets would be to limit their effective length by adding radial venting channels connecting the annular space with the bulk volume of the helium vessel.

The peak pressure as a function of the annular space has a minimum. Then the annular space is less than the annular space at the minimum, the peak pressure is governed by frictional pressure drop and increases in inverse proportion to the annular space. If the annular space is large there is no longer any major frictional pressure drop along the annular, giving uniform pressure rise in the whole magnet.
The measurements on the short twin aperture dipole model verify the increase of the peak pressure with decreasing annular space.

The simulation model of the INFN 2 dipole cannot effectively represent the measured pressure transients. The measurements show that the pressure in the annular space and in the two end reservoirs rises uniformly and begins to decrease when the relief valve is fully open. The simulated pressure transient in the annular space is well in accordance with the measurement, but it is not controlled by the opening of the relief valve. The simulated pressure rise in the two end reservoirs shows the same behaviour as in the TAP magnet, and there is not uniform pressure rise in the magnet.
There is obviously a difference in magnet design between the TAP and the INFN 2 magnet, resulting in completely different quench pressure behaviour. The uniform pressure rise in the INFN 2 magnet is probably due to radial venting of helium from the annular space through the laminated collars and yoke, followed by longitudinal venting through holes in the yoke structure to both the end reservoirs. Since the quench pressure in the INFN 2 is much less than in the TAP magnet and can be controlled by the opening of the relief valve, the differences in magnet design are very positive. Some of

the differences in magnet design which could explain the possibility of radial venting in the INFN 2 magnet and the obstruction in the TAP magnet are discussed in §4.4.

ACKNOWLEDGEMENTS

I would like to thank Philippe Lebrun for giving me the opportunity of working at CERN during these past two years and for proposing a very interesting and challenging project.

Special thanks to Rob van Weelderen for all his help and support in this project and for many fruitful discussions.

I would also like to thank Felix Rodriguez Mateos in the AT-MA group for his valuable contributions concerning the quench propagation process.

REFERENCES

[1] The LHC Study Group, "Design Study of the Large Hadron Collider (LHC), A multiparticle collider in the LEP Tunnel", CERN 91-03, (1991)

[2] Brue, L., Modelisation d'ecoulements transitoires d'helium cryogenique en conduite: application aux transitions resistives des aimants supraconducteurs du LHC, CERN Internal Note LHC 224, (1993)

[3] Patankar, S.V., "Numerical Heat Transfer and Fluid Flow", Hemisphere Publishing Corporation, (1980)

[4] Haaland, S.E. "Simple and explicit formulas for friction factor in turbulent pipe flow", J. Fluids Engng 105, 89-90, (1983).

[5] CRYODATA Inc., P.O. Box 558, Niwot, Colorado 80544, USA

[6] Boissat C., Jagel E., Lee G. and Renshall H.,"CSF User Guide", CERN, version 1.2, February (1992)

[7] Hagedorn, D., Lebrun, Ph., Leroy, D., Perin, R., Vlogaert, J., McInturff, A., "Design and Construction of a Twin-Aperture Prototype Magnet for the CERN LHC Projet", CERN Internal Note SPS/89-30 (1989) and 11th International Conference on Magnet Technology, Tsukuba, Japan (1989)

[8] Granier, M., Hagedorn, D., Henrichsen, K.N., Lebrun, Ph., Leroy, D., Perin, R., Vlogaert, J., Deregel, J., Genevey, P., Jacquemin, J.P., Kircher, F., Le Bars, J., "Performance of the Twin-Aperture Dipole for the CERN LHC", CERN Internal Note AT-MA/9204 (1992) and 1992 EPAC Conference, Berlin

[9] Bona, M., Leroy, D., Perin, R., Rohmig, P., Szeless, B., Thomi, W., "Design, fabrication variants and results of LHC twin-aperture models", IEEE Transactions on Magnetics vol. 28, 338-341, (1992)

NOTATIONS

A	cross-section
D_h	hydraulic diameter
I	current
k	thermal conductivity
L	self inductance
M	mutual inductance
P	pressure
Q	power dissipation in the windings
q_c	power transfer by thermal conduction per unit area
R	resistance
Re	Reynolds number
S	heat transfer area
t	time
T	temperature
u	velocity
x	spatial coordinate
U	voltage
Δx	length of control volume

Greek notation :

α	multiplication factor
δ	thickness
ε	roughness
λ	flow friction coefficient
ξ	loss coefficient for abrupt cross-section changes
ρ	density
φ	internal power conversion per unit volume
ω	power convection from the tube wall to the fluid per unit volume

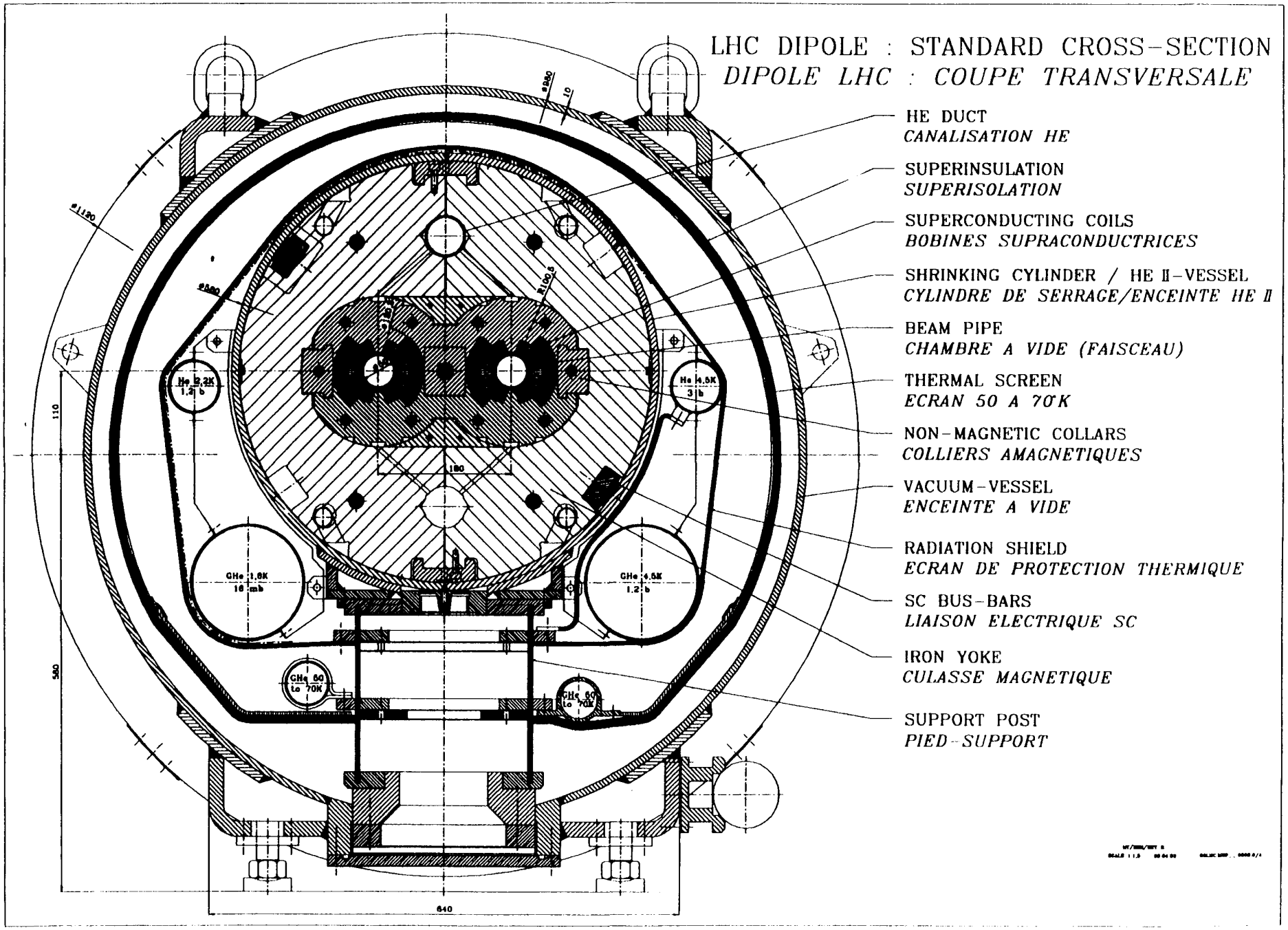
LHC DIPOLE : STANDARD CROSS-SECTION
DIPOLE LHC : COUPE TRANSVERSALE
HE DUCT
CANALISATION HE
SUPERINSULATION
SUPERISOLATION
SUPERCONDUCTING COILS
BOBINES SUPRACONDUCTRICES
SHRINKING CYLINDER / HE II-VESSEL
CYLINDRE DE SERRAGE/ENCEINTE HE II
BEAM PIPE
CHAMBRE A VIDE (FAISCEAU)
THERMAL SCREEN
ECRAN 50 A 70°K
NON-MAGNETIC COLLARS
COLLIERS AMAGNETIQUES
VACUUM-VESSEL
ENCEINTE A VIDE
RADIATION SHIELD
ECRAN DE PROTECTION THERMIQUE
SC BUS-BARS
LIAISON ELECTRIQUE SC
IRON YOKE
CULASSE MAGNETIQUE
SUPPORT POST
PIED-SUPPORT
640

Appendix A